Faculty of Physics
Sofia University “St. Kliment Ohridski”

Radostina Zheleva

Structure and astrophysics of self-gravitating objects in multiscalar theories

SUMMARY

of a thesis for the award of the educational and scientific degree
"‘Doctor"’

Professional direction 4.1 Physical sciences
Scientific specialty: 01.03.01 Theoretical and mathematical physics

Supervisor:
Prof. Stoytcho Yazadjiev

Sofia • 2022

The doctoral student is enrolled in full-time doctoral studies at the Department of Theoretical Physics at the Faculty of Physics of SU "St. Kliment Ohridski". The thesis research was conducted at the Faculty of Physics of Sofia University.

The thesis consists of 73 pages divided into 3 chapters. It contains 17 figures and the bibliography covers 136 titles.

The thesis was discussed at a meeting of the departmental council in the Department of Theoretical Physics of the Faculty of Physics, SU "St. Kliment Ohridski", held on 14.12.2022, and referred for defense with scientific jury with members:

Prof. D.Sci. Angela Slavova Popivanova, IMI-BAS,
Accos. Prof. D.Sci. Lilia Kirilova Anguelova, INRNE-BAS,
Assoc. Prof. PhD Sava Dimitrov Donkov, IA and NAO-BAS,
Prof. D.Sci. Radoslav Hristov Rashkov, Faculty of Physics, Sofia University,
Accos. Prof. PhD Galin Nikolaev Gyulchev, Faculty of Physics, Sofia University.

Contents

Relevance of the topic, purpose and tasks of the thesis

Recent direct detections of gravitational waves from various binary sources have paved the way for gravitational-wave astronomy, which in turn, combined with electromagnetic observations, forms multimessenger astronomy. Multimessenger astronomy is a powerful tool for studying the universe, with great hopes for unraveling many mysteries in Nature, such as dark matter and dark energy, as well as searching for new fundamental fields and new exotic objects. Although general relativity is in brilliant agreement with all observations to date, there are reasons to go beyond the accepted model of gravity in search of new fundamental physics. It is scalar fields that are the simplest to consider, and they appear naturally in extensions of the Standard Model in particle physics and in alternative theories of gravity. In these theories, gravity is described both by the metric tensor and by one or more scalar fields. Of great interest to modern physics are theories with scalar fields coupled to the curvature of space-time, to which the multiscalar Gauss-Bonnet theories also belong. These theories predict the existence of new phenomena, such as spontaneous scalarization of black holes and neutron stars, as well as new types of objects such as space tunnels without the need for exotic matter. This in turn gives rise to new interesting astrophysics related to these objects. The aim of the present thesis is to show the existence of scalarized self-gravitating compact objects supporting non-trivial scalar fields in multiscalar theories of gravity and especially in Einstein-Gauss-Bonnet gravity, where scalar fields interact with space-time curvature through the Gauss-Bonnet topological invariant. In particular, the present thesis numerically demonstrates the existence of scalarized black holes and neutron stars with a rapidly decreasing "scalar hair" in multiscalar Gauss-Bonnet theories, whose scalar space is a maximally symmetric three-dimensional Riemannian space. Constructing these solutions makes it possible to probe the astrophysics around them in order to search for astrophysical effects with a pronounced signature of the scalar fields that could be observed with the next generation of gravity detectors and/or electromagnetic telescopes. As a clear example, quasi-periodic oscillations from accretion disks around rotating space-tunnels have been studied, analyzing the differences with similar oscillations for Kerr black holes, which would help distinguish the two types of self-gravitating objects in future observational missions. Currently, a new generation of spectrometers is being prepared, such as the eXTP (China), STROBE-X (NASA) and LOFT (ESA) missions, which will have extremely high accuracy in measuring the frequencies of quasi-periodic oscillations and will be fully capable of detecting clear signs about the existence of fundamental scalar fields and new exotic objects.

Structure of the thesis

In Chapter 1, the results of the study of the quasi-periodic oscillations of accretion disks around rotating space-time tunnels are presented. The stability of circular orbits in the equatorial plane is discussed and analytical formulas for the epicyclic frequencies are presented. A comparative analysis is made with the case of Kerr black holes.

Chapter 2 introduces multiscalar Einstein-Gauss-Bonnet gravity through its action. Then the dimensionally reduced field equations describing black holes in the theory under the relevant assumptions are presented. Numerically constructed solutions describing black holes as well as their physical characteristics such as horizon area, entropy and the radius of the photon sphere are also given.

Chapter 3 is devoted to neutron stars in multiscalar Einstein-Gauss-Bonnet gravity. The dimensionally reduced field equations describing the structure of neutron stars in the theory are presented. Numerical solutions for neutron stars and the basic dependences such as mass–central density, mass–radius of the star, and binding energy–baryon mass are also presented.

1 Quasi-periodic oscillations from an accretion disk around rotating traversable space-time tunnels

X-ray spectroscopy is a promising tool for testing gravity in the strong-field regime by studying the emission from accretion disks around compact objects. Various features of the X-ray flux will be measured with high precision by the next generation of X-ray satellites such as LOFT [1], eXTP [2], or STROBE-X [3], in particular the quasi-periodic oscillations (QPO) of the accretion flow. Quasi-periodic oscillations are experimentally detected in the X-ray flux from a number of low-mass binary systems, including neutron stars or black holes, as well as several supermassive active galactic nuclei. These represent a number of characteristic peaks appearing in the X-ray spectrum from the compact object, including a low frequency (Hz) signal and a pair of high frequency (kHz) oscillations.

The exact physical mechanism for the formation of the quasi-periodic oscillations is currently unknown, but some features suggest that they are a hydrodynamic phenomenon rather than a manifestation of kinematic effects in the accretion disk such as Doppler modulation of isolated hot spot flows. One such example is the discovery of the correlation between the low- and high-frequency quasi-periodic oscillations, which results in their ratio remaining stable among different X-ray sources[4]-[5]. This motivates the development of disk seismological models that explain QPOs by means of certain captured modes of disk oscillations [6, 7, 8]. Furthermore, observations show that the high-frequency scale of the QPO is inversely proportional to the mass of the compact object and that the pair of peaks follows a constant ratio 3 : 2. Thus, we obtain indications that high-frequency QPOs are caused by relativistic effects, so that they represent a suitable probe of the background space-time. The characteristic frequency ratio of two integers further suggests that the source of the quasi-periodic oscillations may be some nonlinear resonant process occurring in the inner disc.

Approximate resonance models have been developed for thin accretion disks that can provide an explanation for the observed high-frequency QPO [9, 10, 11, 12]. If we assume that the fluid trajectories in the accretion disc follow approximately circular geodesic orbits lying in one plane, we can relate two epicyclic frequencies to their dynamics. They describe the oscillations of circular motion in radial and vertical directions, respectively. In a linear approximation, the radial and vertical oscillations can be considered independent and can be represented as two decoupled harmonic oscillations. However, nonlinear effects cause interactions between the two modes of oscillation, and different types of resonances can be induced when epicyclic frequencies or linear combinations thereof are in the ratio of two integers. Depending on the physical process taking place in the accretion disk, the resonances can be caused by both orbital coupling and one of the epicyclic motions.

Quasi-periodic oscillations are also used as a tool to test gravitational theories in a number of recent scientific works [13, 14, 15, 16, 17, 18, 19, 20, 21]. The properties of epicyclic frequencies depend strongly on the structure of spacetime and can lead to observational effects that can distinguish alternative theories of gravity in the strong-field regime.If the observational data are modeled correctly, QPOs can provide evidence for the existence of more exotic compact objects such as space-time tunnels and naked singularities. The aim of our work is to investigate the quasi-periodic oscillations for a class of rotating traversable space-time tunnels by applying the resonance models and to estimate some of their characteristics, which may be important for observations.

Space-time tunnels are one of the significant predictions of gravitational theories that have yet to be confirmed observationally. In classical General Relativity, the existence of traversable space-time tunnels requires the violation of the isotropic energy condition [22, 23, 24]. However, in quantum gravity this problem is solved naturally, since quantum fields can naturally provide the necessary negative energy density. Alternatively, traversable space-time tunnels arise in

some modified theories of gravity such as Gauss-Bonnet or $f(R)$ theories, where the energy conditions are violated by the gravitational interaction itself without the need for additional fields and matter [25, 26, 27, 28, 29, 30, 31, 32]. They can also exist in a mixed system with another compact object such as a boson or neutron star [33, 34, 35, 36, 37, 38, 39, 40] . Thus, the idea that space-time tunnels can form in nature is reasonably well supported by theoretical arguments, and one of the goals of the next generation of gravitational experiments is to look for evidence of their existence.

The purpose of this chapter is to explore additional observable effects in the electromagnetic spectrum that may distinguish space-time tunnels from other compact objects by studying the high-frequency quasi-periodic oscillations in the tunnel space. For this purpose, we consider a class of geometries constructed by Teo that describes a general stationary and axisymmetric space-time tunnel [24]. Teo rotating tunnel geometry is a generalization of the static spherically symmetric Morris-Thorn spacetime tunnel [41], following the same idea.

1.1 Rotating space-time tunnels

The general class of geometries that describes a stationary axisymmetric space-time tunnel is derived by Teo in the form [24]

$$ds^2 = -N^2 dt^2 + \left(1 - \frac{b}{r}\right)^{-1} dr^2 + r^2 K^2 \left[d\theta^2 + \sin^2\theta \left(d\phi - \omega dt\right)^2\right], \tag{1}$$

where all metric functions depend only on the spherical coordinates r and θ, and are regular on the symmetry axis $\theta = 0, \pi$. The metric function N is related to the gravitational redshift, K is a measure of the radial distance with respect to the origin, ω is related to the spin of the space-time tunnel, while b defines the shape of the throat of the tunnel.

Here we consider the class of geometries where the metric functions N, K, b, and ω depend only on the radial coordinate. This case is of particular physical importance because the geodesic equations that define the propagation of particles and light become integrable. To illustrate some characteristic effects for space-time tunnel geometries, we choose a certain metric that is simple enough but still representative of the class. We set the shape function and the radial distance function to be equal to the constants, while for the rest of the metric functions we take

$$N = \exp\left(-\frac{r_0}{r}\right), \qquad \omega = \frac{2J}{r^3}, \qquad b = r_0, \qquad K = 1. \tag{2}$$

Thus, the mass of the space-time tunnel is equal to $M = r_0$. We can further introduce a rotation parameter $a = J/M^2$ and represent the metric in dimensionless form by doing the conformal transformation and rescaling

$$dS^2 = r_0^{-2} ds^2, \qquad t \to r_0 t, \qquad r \to r_0 r.$$

In this way, we obtain a solution of the spacetime tunnel with a unit mass and a throat located at $r = 1$.

1.2 Circular orbits in the equatorial plane

For any stationary and axisymmetric metric, we can derive some general expressions that define the kinematic quantities of circular orbits in the equatorial plane. Let us consider the general form of the metric

$$ds^2 = g_{tt}\, dt^2 + 2g_{t\phi}\, dt d\phi + g_{rr}\, dr^2 + g_{\theta\theta}\, d\theta^2 + g_{\phi\phi}\, d\phi^2, \tag{3}$$

and denote the specific energy and angular momentum of the particles by E and L, respectively. Since we have two Killing vectors with respect to time translations and rotations about the axis of symmetry, energy and angular momentum are conserved on the geodesics. In addition, on each geodesic trajectory we have the constraint $g_{\mu\nu}\dot{x}^\mu\dot{x}^\nu = \epsilon$, where ϵ takes the value $\epsilon = -1$ for a time-like geodesic, and $\epsilon = 0$ for a null geodesic. Choosing an affine parameter τ we can express the time-like geodesic equations in the equatorial plane as

$$\begin{aligned}
\frac{dt}{d\tau} &= \frac{Eg_{\phi\phi} + Lg_{t\phi}}{g_{t\phi}^2 - g_{tt}g_{\phi\phi}}, \\
\frac{d\phi}{d\tau} &= -\frac{Eg_{t\phi} + Lg_{tt}}{g_{t\phi}^2 - g_{tt}g_{\phi\phi}}, \\
g_{rr}\left(\frac{dr}{d\tau}\right)^2 &= -1 + \frac{E^2g_{\phi\phi} + 2ELg_{t\phi} + L^2g_{tt}}{g_{t\phi}^2 - g_{tt}g_{\phi\phi}}.
\end{aligned} \tag{4}$$

In the last equation, we can introduce an effective potential V_{eff} given by

$$V_{eff} = -1 + \frac{E^2g_{\phi\phi} + 2ELg_{t\phi} + L^2g_{tt}}{g_{t\phi}^2 - g_{tt}g_{\phi\phi}}. \tag{5}$$

The qualitative behavior of the radial motion is completely determined by the properties of the effective potential. In particular, circular orbits correspond to its fixed points

$$V_{eff}(r) = 0, \qquad V_{eff,r}(r) = 0, \tag{6}$$

where the comma means the derivative with respect to the radial coordinate. Solving this system of equations we can obtain formulas for the specific energy and angular momentum on the circular orbits, namely

$$E = -\frac{g_{tt} + g_{t\phi}\omega_0}{\sqrt{-g_{tt} - 2g_{t\phi}\omega_0 - g_{\phi\phi}\omega_0^2}}, \tag{7}$$

$$L = \frac{g_{t\phi} + g_{\phi\phi}\omega_0}{\sqrt{-g_{tt} - 2g_{t\phi}\omega_0 - g_{\phi\phi}\omega_0^2}}. \tag{8}$$

For angular velocity, we get accordingly

$$\omega_0 = \frac{d\phi}{dt} = \frac{-g_{t\phi,r} \pm \sqrt{(g_{t\phi,r})^2 - g_{tt,r}g_{\phi\phi,r}}}{g_{\phi\phi,r}}, \tag{9}$$

where the signs $+/-$ correspond to orbital motion in the direction of rotation of the compact object or in the opposite direction.

Timelike circular orbits exist in the region where energy and angular momentum are well defined. The curves where they become divergent correspond to the location of the null circular orbits, i.e. the photon rings. They give the boundary of the region of existence of time-like circular orbits. If only an unstable photon ring is present, the domain of existence of the time-like circular orbits is simply-connected, and for an asymptotically flat spacetime, the location of the photon ring gives its lower bound in the radial direction. If there are multiple photon rings, the domain of existence may consist of several disconnected parts, i.e. the circular orbits will be located in several annular regions with spaces between them.

Calculating the kinematics for the space of a traversable space-time tunnel (1), we obtain the expressions

$$\begin{aligned}
\omega_0 &= \omega + \frac{r^2K^2\omega_{,r} \pm \sqrt{N^2_{,r}(r^2K^2)_{,r} + r^4K^4(\omega_{,r})^2}}{(r^2K^2)_{,r}}, \\
E &= \frac{N^2 + r^2K^2\omega(\omega_0-\omega)}{\sqrt{N^2 - r^2K^2(\omega_0-\omega)^2}}, \\
L &= \frac{r^2K^2(\omega_0-\omega)}{\sqrt{N^2 - r^2K^2(\omega_0-\omega)^2}},
\end{aligned} \tag{10}$$

where we have the sign $+/-$ orbits in the direction of rotation of the compact object or opposite. In the region there exist time-like circular orbits for which the inequality $N^2 - r^2K^2(\omega_0-\omega)^2 > 0$ is satisfied.

In Figure 1 we show the region of existence of the circular orbits for the particular space-time tunnel solution given by (2). The rotating solution of a space-time tunnel exists for any values of the rotation parameter. However, since our goal is to make a comparison with the Kerr black hole, we restrict ourselves to the interval $a \in [0, 1]$. To illustrate the behavior of circular orbits in a direction opposite to the rotation of the compact object, we include negative values of the rotation parameter $a \in [-1, 0)$. The prograde circular orbits exist throughout the space around the throat of the space-time tunnel. On the other hand, counter-rotating particles are pushed away from the rotating compact object and can only reach a certain radial distance, leaving a region around the throat of the space-time tunnel where counter-rotating circular orbits are not allowed.

1.3 Stability of circular orbits in the equatorial plane

We consider the geodesic equations in the equatorial plane

$$\ddot{x^\alpha} + \Gamma^\alpha_{\beta\gamma}\dot{x^\beta}\dot{x^\gamma} = 0\,, \tag{11}$$

and we make a small perturbation of the circular motion $\tilde{x}^\mu(s) = x^\mu(s) + \xi^\mu(s)$ where $x^\mu(s)$ denotes the circular orbit and s is the affine parameter on the geodesic. Working in the linear approximation we can obtain the following system for the deviation $\xi^\mu(s)$ [42], [43]

$$\begin{aligned}
&\frac{d^2\xi^\mu}{dt^2} + 2\gamma^\mu_\alpha\frac{d\xi^\alpha}{dt} + \xi^b\partial_b\mathcal{V}^\mu = 0\,, \quad b = r, \theta \\
&\gamma^\mu_\alpha = \left[\Gamma^\mu_{\alpha\beta}u^\beta(u^0)^{-1}\right]_{\theta=\pi/2}\,, \\
&\mathcal{V}^\mu = \left[\gamma^\mu_\alpha u^\alpha(u^0)^{-1}\right]_{\theta=\pi/2}\,,
\end{aligned} \tag{12}$$

where $u^\mu = u^0(1, 0, 0, \omega_0)$ is the 4-velocity vector, ω_0 is the orbital frequency.

From the perturbation equations of the circular orbits, we can obtain the epicyclic frequencies for the rotating traversable space-time tunnels

$$\omega^2_\theta = (\omega_0 - \omega)^2\,, \tag{13}$$

$$\begin{aligned}
\omega^2_r = {} & \frac{(b-r)}{rN^2}\left[\omega^2_\theta\, r^4K^4\omega^2_{,r} + rK^2(\omega_0-\omega)(2r(N^2\omega_{,r})_{,r} - 3N^2(r\omega_{,r})_{,r})\right] \\
& + \omega^2_\theta\,(b-r)\left[\frac{K}{r}(r^2K_{,r})_{,r} - 3K_{,r}(rK)_{,r}\right] \\
& - \frac{(b-r)}{r^2}\left[3NN_{,r} + rNN_{,rr} - 3r(N_{,r})^2\right]\,,
\end{aligned} \tag{14}$$

where we restrict ourselves to the class of solutions with metric functions N, K, b, and ω in depending only on r, and the orbital frequency ω_0 is given by eq. (10).

From these expressions we can derive some general properties of the tunnel geometries under consideration. We see that for all solutions of the tunnel the vertical epicyclic frequency is always positive, so the circular orbits are always stable with respect to vertical perturbations. Thus, the linear stability is determined only by the radial epicyclic frequency, similar to the case for the Kerr black hole. In a static limit, we get that the vertical epicyclic frequency coincides with the Schwarzschild black hole-like orbital frequency. Thus, circular motion is characterized by only two independent quantities.

To gain further intuition about the behavior of circular orbits, we consider the stability region for the particular tunnel solution given by Eq.(2). In Figure 1 we present the curve on which the radial epicyclic frequency vanishes, thus separating the stability region of the circular orbits. In the region above the curve and to its right, the inequality $\omega_r^2 > 0$ is satisfied, so this part of space-time represents the region of stability of time-like circular orbits in the equatorial plane.

We see that for most of the spin parameters in the interval $a \in [0, 1]$ the orbits rotating in the direction of the tunnel are stable in the whole space. For small angular momentum of the space-time tunnel, however, we obtain a qualitatively different situation. The $\omega_r^2 = 0$ curve has a maximum at $a = 0.0167$ and crosses the tunnel throat at $a = 0.0144$. Then, in the interval $a \in (0.0144, 0.0167)$ the stability region consists of two disconnected parts, separated by a region where circular orbits become unstable. For each spin parameter $a \in (0.0144, 0.0167)$, the region of instability is bounded by two marginally stable circular orbits located at radii that correspond to the solutions of the equation $\omega_r^2 = 0$. As the angular momentum increases, the region of instability becomes smaller, while at $a = 0.0167$ it disappears completely. These configurations have astrophysical applications as they lead, for example, to a discontinuity in the accretion disc within the thin disc model. In this case, the accretion disk consists of two annular regions separated by a gap.

For the counter-rotating orbits as well as the static solution for the space-time tunnel, the region of stability resembles the Kerr black hole case. There is an innermost stable circular orbit (ISCO) located at the radial distance r_{ISCO} where the radial epicyclic frequency becomes zero, and all orbits at higher values of the radial coordinate are stable ISCO takes its closest position to the tunnel throat in a static boundary located at $r/r_0 = 2$. As the angular momentum of the tunnel increases, it moves away to larger radii.

1.4 Properties of epicyclic frequencies

Epicyclic and orbital frequencies are the main quantities used in the development of geodetic models for the quasi-periodic oscillations of the accretion disk such as the orbital precession model and the resonance models. Therefore, their properties determine important features of the model such as the possible types of resonances that can be excited, the radial distance from the compact object where the resonance process takes place, and the values of the observed peak frequencies.

In this section we will investigate the epicyclic frequencies of a space-time tunnel, making a comparison with a Kerr black hole. For the Kerr black hole, we observe only a slight variation in the behavior of the characteristic frequencies over the entire range of the spin parameter $a \in [0, 1]$. The orbital frequency is a monotonically decreasing function for each value of the spin parameter and the radial coordinate. The radial epicyclic frequency always has a single maximum, while the vertical is a monotonically decreasing function for slow-rotating black holes and obtains a single maximum for fast-rotating black holes. In addition, for any value of the spin parameter, the orbital frequency is always greater than the vertical epicyclic frequency, which in turn is greater than the radial one. Thus, we have $\omega_0^2 > \omega_\theta^2 > \omega_r^2$ for the entire range

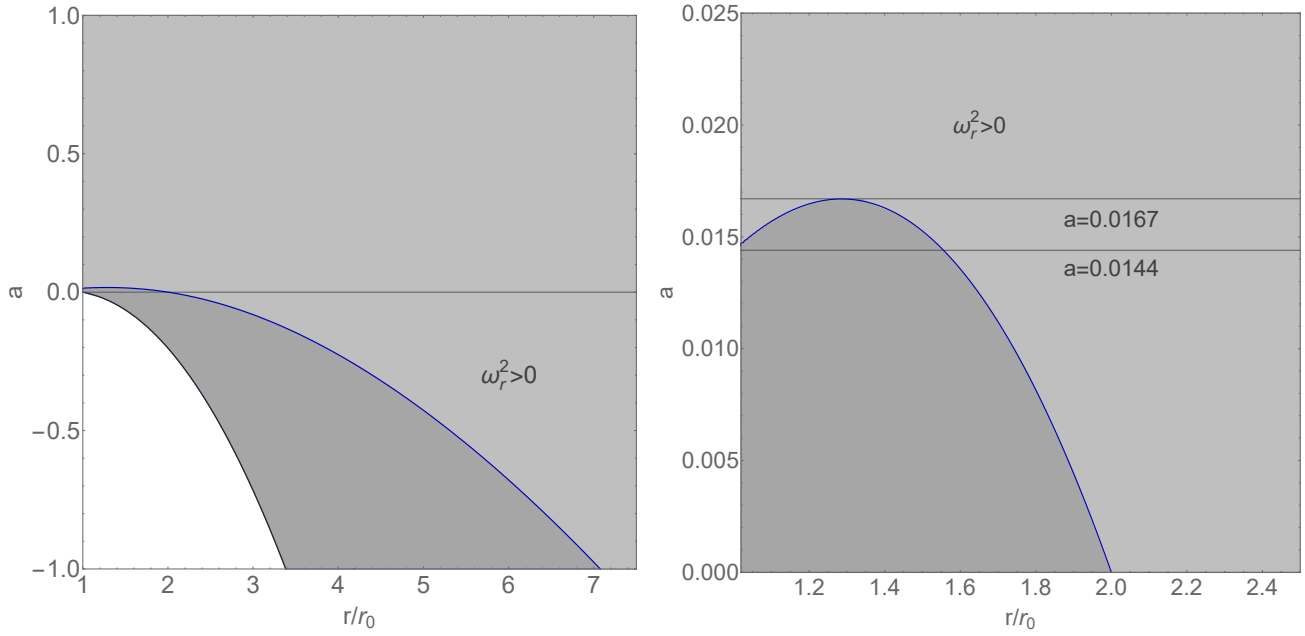

a) *b)*

Figure 1: Existence and stability of circular orbits in the equatorial plane for rotating traversable space-time tunnels. The gray curve indicates the location of the null circular orbits, while $\omega_r^2 = 0$ is satisfied on the blue curve. Timelike circular orbits exist in the gray region, and they are stable in the light gray region bounded by the blue curve. Positive values of the spin parameter represent co-rotating circular orbits, while negative values correspond to counter-rotating ones.

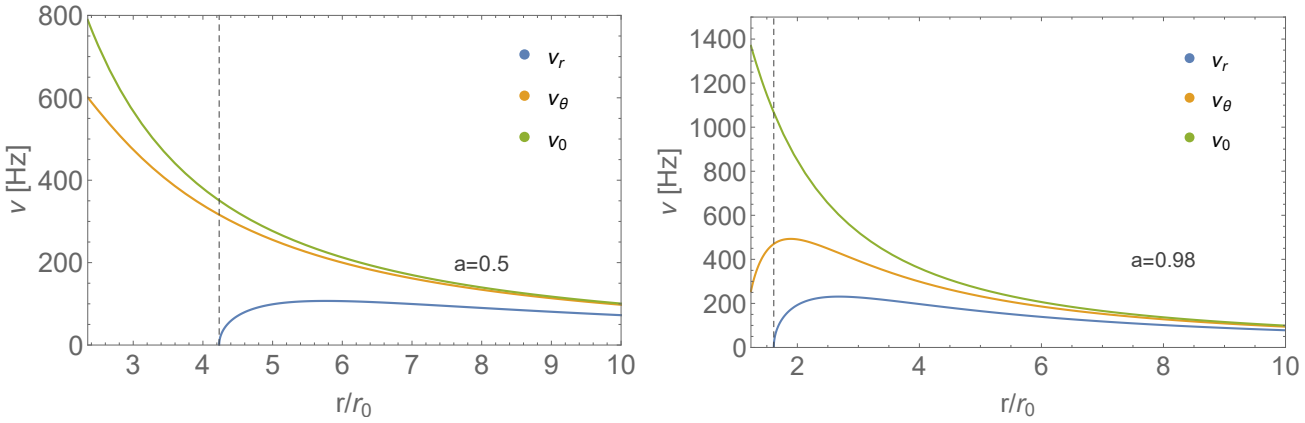

a) *b)*

Figure 2: Examples of the qualitatively different types of epicyclic frequency behavior for the Kerr black hole. For slow rotation, the vertical epicyclic frequency is a monotonically decreasing function, while for faster rotations it has a single maximum. The radial coordinate takes values larger than the photon orbit, and the location of the ISCO is given by a dashed line.

of the radial coordinate over the photon orbit. The frequency behavior for the Kerr black hole is demonstrated in Figure 2 for some characteristic values of the spin parameter for the two qualitatively different cases.

Besides sharing some similarities with the Kerr black hole, the epicyclic frequencies for space-time tunneling also show major differences. One important difference is that different arrangements of orbital and epicyclic frequencies can be realized. This allows for a much more diverse range of resonant excitation scenarios, some leading to stronger observable signals. In Figure 3 we illustrate the possible cases for the particular solution of a space-time tunnel (2) by presenting the curves $\omega_r^2 = \omega_\theta^2$ and $\omega_r^2 = \omega_0^2$. In the upper region bounded by each of

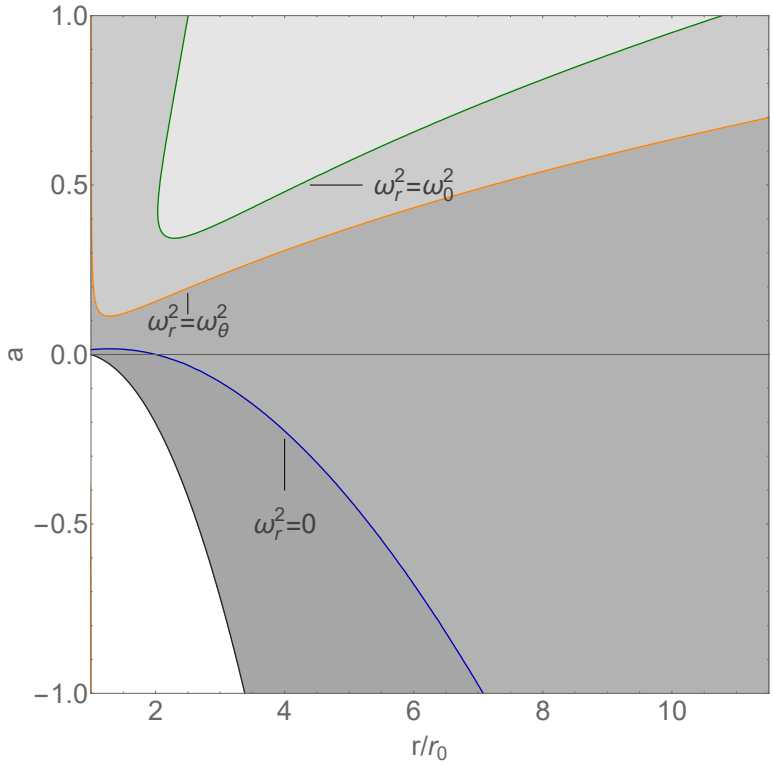

Figure 3: Arrangement of orbital and epicyclic frequencies for rotating traversable space-time tunnels. The curve $\omega_r^2 = \omega_\theta^2$ is drawn in orange, while the curve $\omega_r^2 = \omega_0^2$ is represented in green. In the region above the orange curve we have $\omega_r^2 > \omega_\theta^2$, and between it and the green curve $\omega_r^2 > \omega_0^2$ is satisfied. For counter-rotating orbits with $a < 0$, it holds that $\omega_\theta^2 > \omega_0^2$, while in the co-rotating case $a > 0$ we have the opposite inequality. The gray and blue curves are the boundaries of the regions of existence and stability of timelike circular orbits, respectively.

the curves, the inequalities $\omega_r^2 > \omega_\theta^2$ and $\omega_r^2 > \omega_0^2$ are satisfied. From the expressions for the epicyclic frequencies (3) we can see that for co-rotating orbits we have $\omega_\theta^2 < \omega_0^2$, while for counter-rotating orbits the opposite case $\omega_\theta^2 > \omega_0^2$ is realized. This result is rather general for traversable tunnels, as it applies to the entire class of tunnels with metric function N , ω , b , and K depending only on r.

The analysis based on Figure 3 shows that the case of counter-rotating orbits resembles the Kerr black hole as it has a uniform frequency ordering $\omega_\theta^2 > \omega_0^2 > \omega_r^2$ for the entire range of the radial coordinate $r \in (r_{ISCO}, \infty)$. For revolving orbits we have different scenarios. In the region above the curve $\omega_r^2 = \omega_0^2$ we have $\omega_r^2 > \omega_0^2 > \omega_\theta^2$, below the curve $\omega_r^2 = \omega_\theta^2$ the inequality $\omega_0^2 > \omega_\theta^2 > \omega_r^2$ is satisfied, while between the two curves we have $\omega_0^2 > \omega_r^2 > \omega_\theta^2$. In a static limit, we get the degenerate case $\omega_\theta^2 = \omega_0^2 > \omega_r^2$ similar to the Schwarzschild black hole. In the next section, we will explore the implications of these types of frequency ordering on the possibilities of forming different resonances.

The next step is to study the behavior of the orbital and epicyclic frequencies as a function of the radial coordinate r for different spin parameters a . For counter-rotating orbits, we again observe a consistent behavior over the entire range of $a \in (0, 1]$, while for co-rotating orbits we have different possibilities depending on the spin rate of the space-time tunnel. In the counter-rotating case, the radial epicyclic frequency always has a single maximum, while the vertical is a monotonically decreasing function of r . Thus, for counter-rotating orbits the tunnel resembles a slowly rotating Kerr black hole. In the prograde case, we can classify the solutions of the spacetime tunnel in terms of the behavior of the epicyclic frequencies into the following categories:

I. a $\in [0, 0.0144)$: The stability region of circular orbits is simply-connected. The radial

epicyclic frequency ω_r has a single maximum, while ω_θ is a monotonically decreasing function.

II. a $\in [0.0144, 0.0167]$: The stability region of circular orbits consists of two disconnected parts. In each of the regions of stable orbits, the radial epicyclic frequency ω_r possesses a single maximum. The vertical epicyclic frequency ω_θ is a monotonically decreasing function.

III. a $\in [0.0167, 0.025]$: The stability region of the circular orbits is simply-connected. The radial epicyclic frequency ω_r has two maxima and a minimum, while ω_θ is a monotonically decreasing function.

IV. a $\in [0.025, 0.029)$: The stability region of the circular orbits is simply-connected. The radial epicyclic frequency ω_r has two maxima and a minimum, while ω_θ possesses one maximum.

V. a $\in [0.029, 1]$: The stability region of circular orbits is simply-connected. Both the radial and vertical epicyclic frequencies possess a single maximum.

We see that the epicyclic frequencies for the counter-rotating case and the very slowly rotating case I. behave like a slowly rotating Kerr black hole, since the static limit resembles a Schwarzschild black hole. Furthermore, we have some exotic regions in the cases II, III and IV with a multicorrelated region of stability of the circular orbits or multiple extrema of the radial epicyclic frequency that do not exist for the Kerr black hole.As the spin parameter is further increased in region V, the epicyclic frequencies begin to behave as for the rapidly rotating Kerr black hole. The orbital frequency is always a monotonically decreasing function of the radial coordinate for both co- and counter-rotating orbits.

In Figure 4 we present the analysis of the behavior of the epicyclic frequencies as a function of r for different values of the rotation parameter through the curves $\partial_r \omega_r = 0$ and $\partial_r \omega_\theta = 0$, as well as the second derivatives $\partial_r^2 \omega_r = 0$, and $\partial_r^2 \omega_\theta = 0$. The regions of qualitatively different types of behavior are bounded by horizontal lines corresponding to the characteristic values of the spin parameter where the transitions occur. We additionally demonstrate examples for each of the classes I. - IV. in Figure 5, where we use the frequencies $\nu_r = \omega_r/2\pi$, $\nu_\theta = \omega_\theta/2\pi$ and $\nu_0 = \omega_0/2\pi$ for some specified values of the spin parameter.

1.5 Nonlinear resonances

In a linear approximation, small deviations from circular geodesic motion are described by two independent harmonic oscillations with their own frequencies, called radial and vertical epicyclic frequencies. However, a more realistic description of the processes in the accretion disc requires the inclusion of additional non-linear terms in the perturbation equations. They provide information on various forces acting in the accreting fluid such as pressure, viscosity, magnetic fields, etc., and lead to the coupling of the two epicyclic modes.Usually, such an interaction between natural frequencies is a prerequisite for the excitation of resonances in dynamic systems, which are realized when the system reaches suitable conditions.

At present, the physical processes involved in the accretion disk are not well understood. It is therefore difficult to derive rigorous expressions for the nonlinear terms governing the behavior of small perturbations. A reasonable approach is to consider some basic types of interactions that are similar enough to occur in many physical situations for a wide range of particular processes.For example, we can consider nonlinear corrections to the perturbation

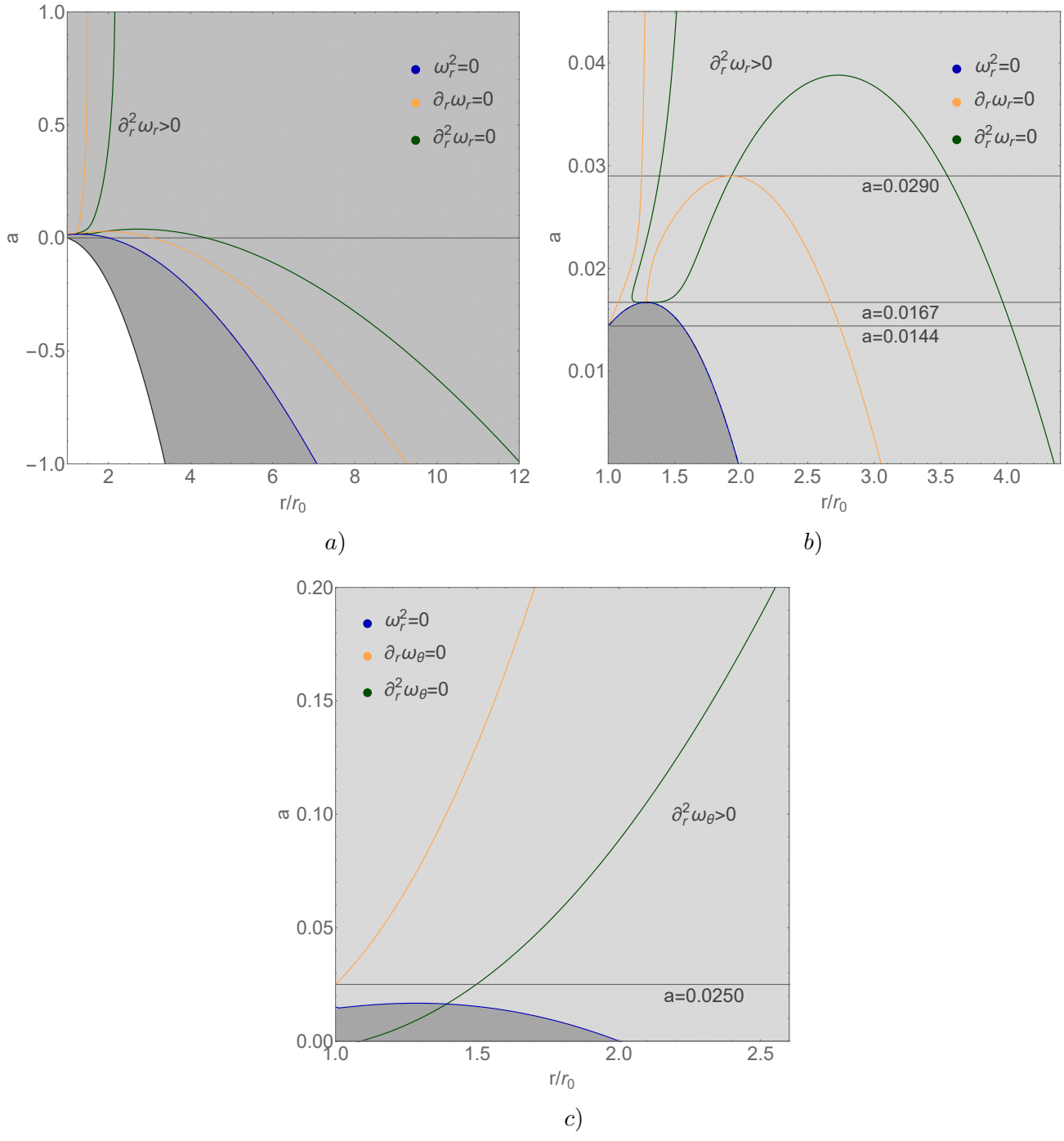

Figure 4: Behavior of the radial epicyclic frequency a) and b), and the vertical epicyclic frequency c) as a function of the radial coordinate. The curves $\partial_r\omega_r = 0$ and $\partial_r\omega_\theta = 0$ are presented in orange, while the second derivatives $\partial_r^2\omega_r = 0$ and $\partial_r^2\omega_\theta = 0$ are represented in green. The functions $\partial_r^2\omega_r$ and $\partial_r^2\omega_\theta$ are positive above and to the right of the green curves. In enlarged section b) we illustrate the regions with different types of behavior of the radial epicyclic frequency for slow rotation, where we indicate the transition values of the rotation parameter with horizontal lines. We additionally show the boundaries of the existence and stability regions of the circular geodesic with gray and blue lines, respectively.

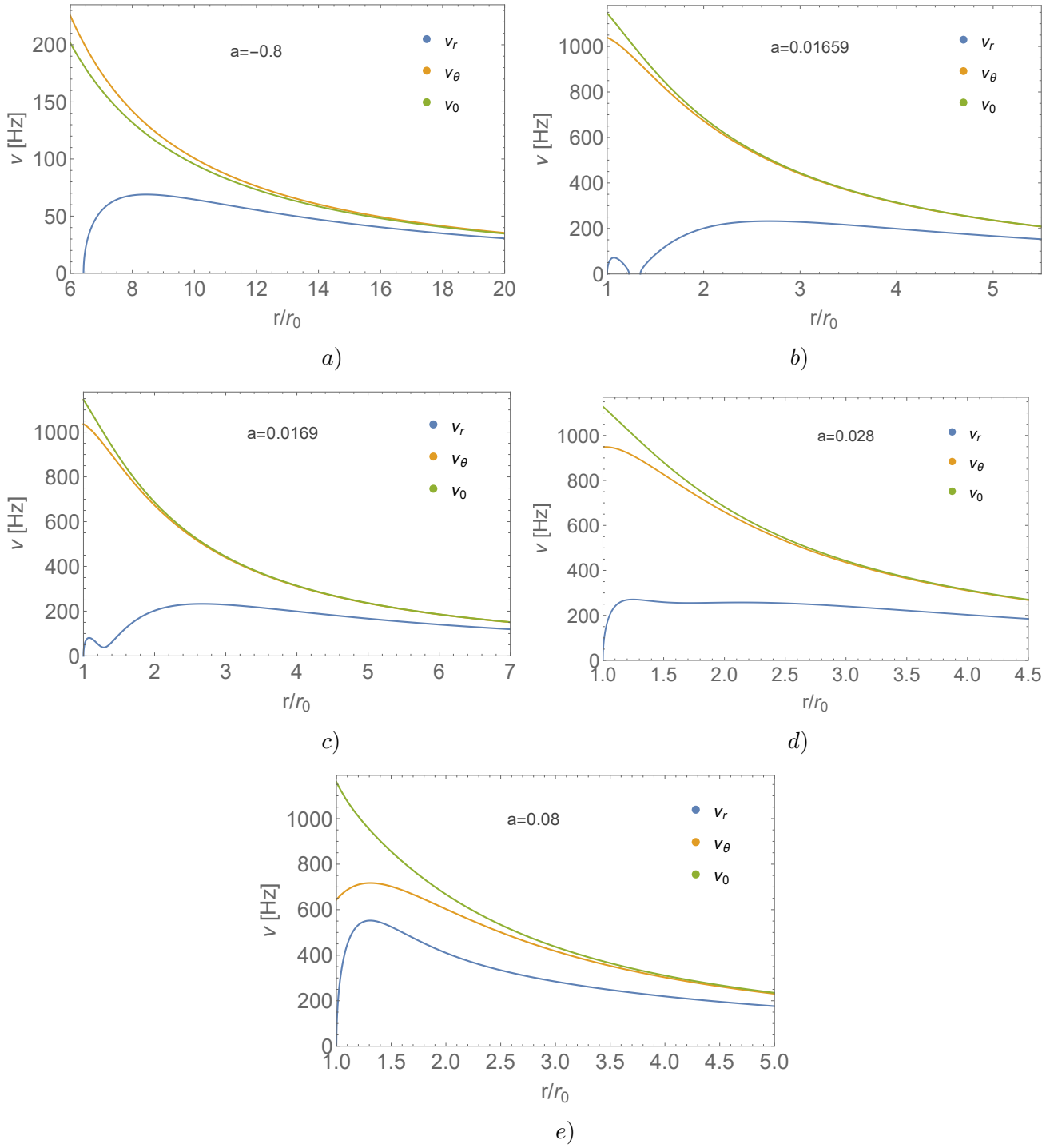

Figure 5: Examples of the qualitatively different types of epicyclic frequency behavior for rotating traversable space-time tunnels.

equations describing the small deviation from a geodesic circular motion of the form

$$\frac{d^2\xi^r}{dt^2} + \omega_r^2 \xi^r = \omega_r^2 f_r \left(\xi^r, \xi^\theta, \frac{d\xi^r}{dt}, \frac{d\xi^\theta}{dt}\right),$$
$$\frac{d^2\xi^\theta}{dt^2} + \omega_\theta^2 \xi^\theta = \omega_\theta^2 f_\theta \left(\xi^r, \xi^\theta, \frac{d\xi^r}{dt}, \frac{d\xi^\theta}{dt}\right), \tag{15}$$

where f_r and f_θ are nonlinear functions. The specific form of these functions should be determined by the properties of the physical model of the accretion flow. However, without resorting to a particular model, we can propose some simple cases that are likely to arise in many scenarios and explore their behavior. One of the simplest situations is to assume that $f_r = 0$ and $f_\theta = h, \xi^r \xi^\theta$, where h is a coupling constant. The equation for vertical oscillations is in the form

$$\frac{d^2\xi^\theta}{dt^2} + \omega_\theta^2 \xi^\theta = -\omega_\theta^2 h \cos(\omega_r t)\xi^\theta. \tag{16}$$

We thus obtain the Mathieu equation, which is known to describe parametric resonances for frequency ratios

$$\frac{\omega_r}{\omega_\theta} = \frac{2}{n}, \tag{17}$$

where n is a positive integer (see e.g. [44]). When the coupling is weak, or $h << 1$, the smallest possible value of n corresponds to the strongest resonance. Although the parametric resonances were obtained by assuming an ansatz for the frequency coupling, they have been shown to be a mathematical property of thin, quasi-Keplerian discs [10], [45], [46].

Another common dynamical system that exhibits resonant behavior is the forced nonlinear oscillator. In this regard, it has been proposed that nonlinear effects in circular orbit perturbations can be described by including a periodic radial force in the equation for the vertical oscillations with a frequency equal to the radial epicyclic frequency. Thus the equation for vertical oscillations becomes

$$\frac{d^2\xi^\theta}{dt^2} + \omega_\theta^2 \xi^\theta + [\text{non linear terms in } \xi^\theta] \;=\; h(r)\cos(\omega_r t). \tag{18}$$

Resonances are excited when epicyclic frequencies are integer ratios $\omega_\theta = n\omega_r$. Since the equation is non-linear, the resonant solution can also contain linear combinations of epicyclic frequencies, which gives additional possibilities for working with the frequencies of quasi-periodic oscillations.

We further discuss how the described resonance phenomena can explain the observed double-peak frequencies in the X-ray flux of accreting compact objects, provided that the compact object is modeled as a rotating traversable space-time tunnel. In resonance models, the two-peak frequencies are explained by identifying them with suitable combinations of resonance frequencies such that the observational ratio between low (ν_L) and high (ν_U) frequencies is satisfied, i.e. $\nu_U : \nu_L = 3 : 2$. In general, identifications with frequencies corresponding to lower-order resonances are preferred because they lead to larger amplitudes of the observed signal. For the parametric resonance, this can be done directly by making the identification $\nu_U = \nu_\theta = \omega_\theta/2\pi$ and $\nu_L = \nu_r = \omega_r/2\pi$. In the case of the Kerr black hole, this is the lowest order parametric resonance, since the $n = 1, 2$ parametric resonances do not exist. If we consider forced resonances, we must identify the observed frequencies with linear combinations of epicyclic frequencies to achieve the $3 : 2$ ratio. For a Kerr black hole, the lowest possible order forced resonances are $n = 2$ and $n = 3$ when epicyclic frequencies are related as $\omega_\theta : \omega_r = 2 : 1$ and $\omega_\theta : \omega_r = 3 : 1$. The observable ratio can be obtained by making the identities

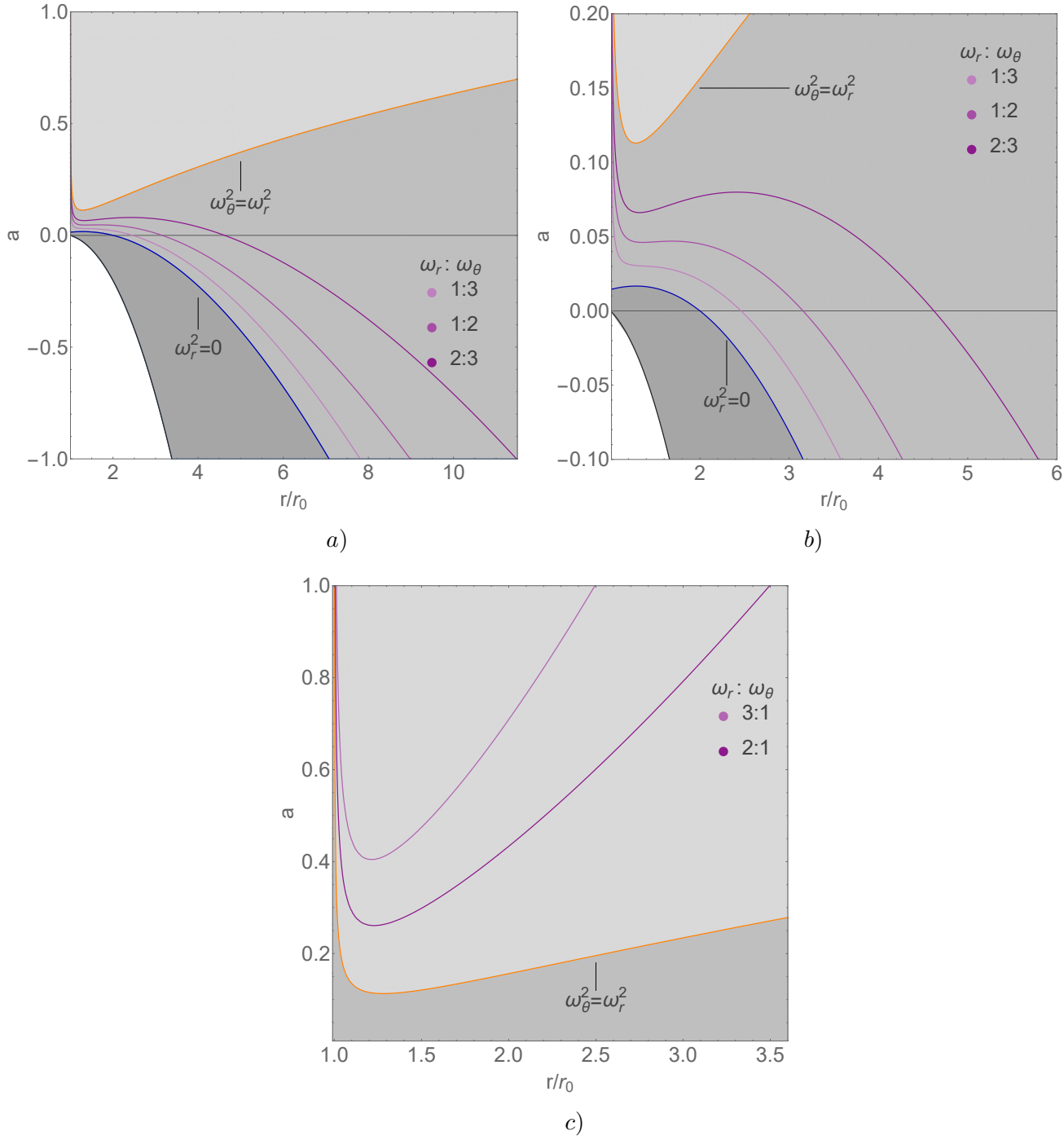

Figure 6: Location of the parametric and forced resonances depending on the spin parameter of the space-time tunnel. In a) and b) we represent the case where the epicyclic frequencies satisfy the inequality $\omega_r < \omega_\theta$, while in c) we have the ordering $\omega_r > \omega_\theta$. In the enlarged section b) we can see the location of the resonances for a static tunnel.

$\nu_U = \nu_\theta + \nu_r = (\omega_\theta + \omega_r)/2\pi$ and $\nu_L = \nu_\theta$, and $\nu_U = \nu_\theta$ and $\nu_L = \nu_\theta - \nu_r = (\omega_\theta - \omega_r)/2\pi$, respectively. The simplest cases of Kepler resonances possible in Kerr black hole spacetime are $\omega_0 : \omega_r = 3 : 2$, $\omega_0 : \omega_r = 2 : 1$, or $\omega_0 : \omega_r = 3 : 1$, and likewise if we consider the coupling between the vertical epicyclic and orbital frequencies.

In the space-time of the tunnel, we get a much richer picture of the possible resonance phenomena. One of the most distinctive features compared to a Kerr black hole is that different types of ordering of orbital and epicyclic frequencies occur in different regions of parameter space. This makes it possible to excite more diverse types of resonances that do not exist in Kerr spacetime. For a Kerr black hole, we always have the inequality $\omega_\theta > \omega_r$. This prevents

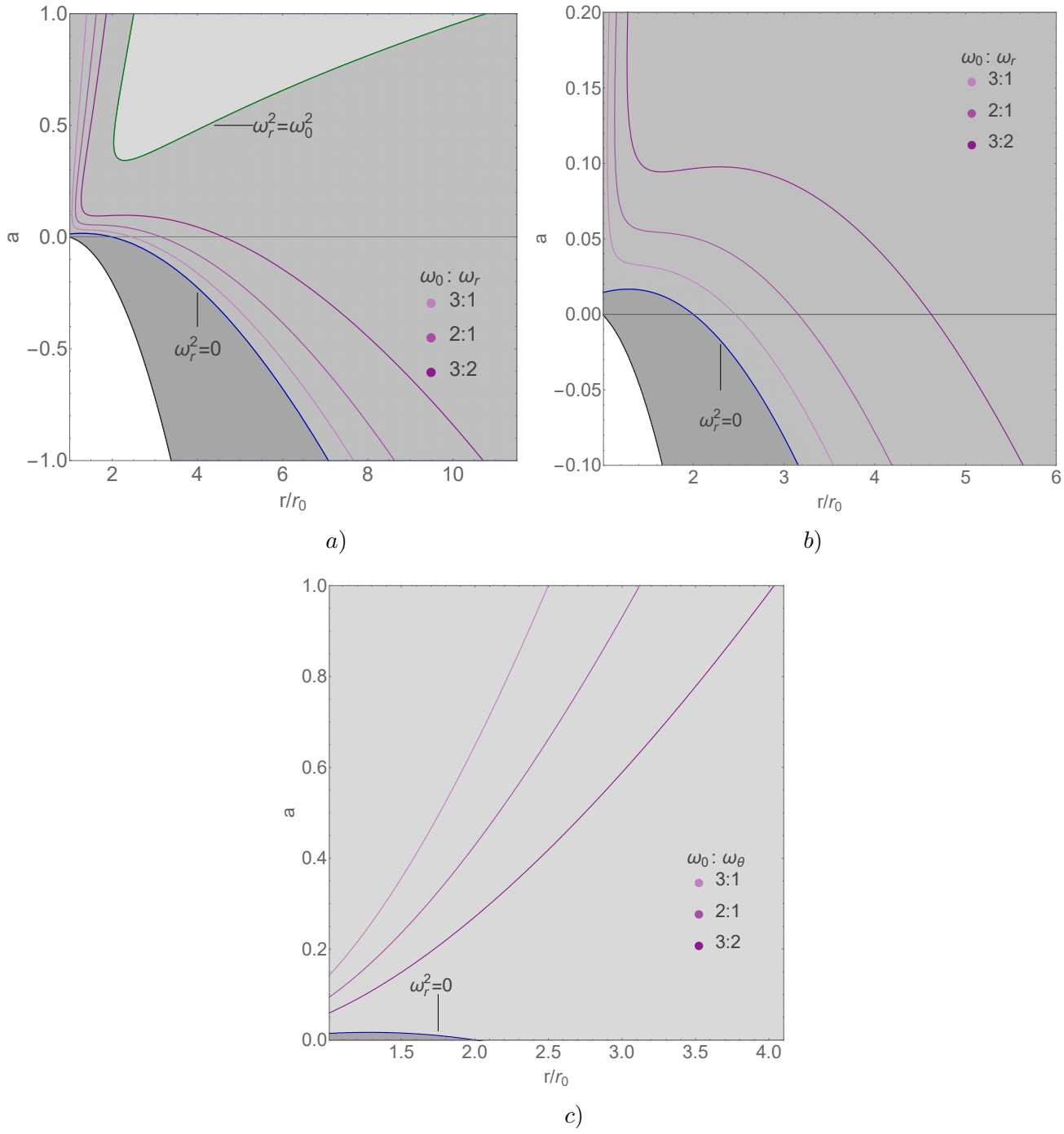

Figure 7: The location of the Kepler resonances as a function of the tunnel spin parameter. In a) and b) (enlarged section) we study the resonances due to the coupling between the radial epicyclic and orbital frequencies, while in c) the coupling is between the vertical epicyclic and orbital frequencies. The lowest order Keplerian resonances do not exist in the regions in the parameter space where $\omega_0 < \omega_r$ or $\omega_0 < \omega_\theta$ is satisfied.

the excitation of the lower-order parametric resonances $n = 1$ and $n = 2$, i.e. $\omega_r = 2\omega_\theta$ and $\omega_r = \omega_\theta$, which would also have the highest amplitudes. In contrast, for the rotating tunnel given by (2), the parametric resonances $n = 1$ and $n = 2$ are possible for any value of the spin parameter $a \in [0, 1]$. The observed $3 : 2$ ratio between the two-peak frequencies can be explained by identifying the low and high observed frequencies ν_L and ν_U as $\nu_U = \nu_\theta + \nu_r$ and $\nu_L = nu_r$ in the case $n = 1$, and $\nu_U = 3\nu_\theta = 3\nu_r$ and $\nu_L = 2\nu_r = 2\nu_\theta$ in the case $n = 2$.

For the excitation of the forced resonances of the lowest order, we get new possibilities when the epicyclic frequencies satisfy the ratios $\omega_\theta : \omega_r = 1 : 2$ and $\omega_\theta : \omega_r = 1 : 3$. These lead to the observable frequencies $\nu_U = \nu_\theta + \nu_r$, $\nu_L = \nu_r$, and $\nu_U = \nu_r$, $\nu_L = \nu_r - \nu_\theta$, respectively. Kepler resonances can be observed for combinations such as $\omega_0 : \omega_r = 3 : 2$ ($\nu_U = \nu_0$, $\nu_L = \nu_r$) , $\omega_0 : \omega_r = 2 : 1$ ($\nu_U = 3\nu_r$, $\nu_L = \nu_0$), or $\omega_0 : \omega_r = 3 : 1$ ($\nu_U = \nu_0$, $\nu_L = 2\nu_r$) in the regions where the ordering $\omega_0 > \omega_r$ is valid and the corresponding cases with coupling between the vertical epicyclic and orbital frequencies when $\omega_0 > \omega_\theta$. Our study shows that the lowest order Keplerian resonances with ratios between the orbital frequency and one of the epicyclic frequencies $m : n$, where $m, n = 1, 2, 3$ do not exist when we have an arrangement $\omega_0 < \omega_r$ or $\omega_0 < \omega_\theta$.

The location of the described resonances as a function of the spin parameter is illustrated in figures 6-7. For the prograde orbits, the resonances are excited in the immediate vicinity of the space-time tunnel throat, i.e. in the region with a very strong gravitational field. Furthermore, this behavior is observed not only for rapidly rotating space-time tunnels, but for a wide range of values of the spin parameter of the space-time tunnel. Thus, quasi-periodic oscillations in tunnel spacetime can be a valuable probe of the strong gravity regime.Another characteristic feature is that for a fixed value of the spin parameter the same type of resonance occurs for several different radii. In the Kerr black hole case, the resonance curves are monotonic and such behavior is ruled out. This phenomenon is particularly interesting because the radius where the resonance is excited is related to the properties of the physical process that causes it. Thus, for the tunnel spacetime we can have the same kind of resonance excited simultaneously in different regions in the accretion disc, possibly caused by different physical processes.

1.6 Conclusion

In this chapter, we explored how we can interpret the high-frequency quasi-periodic oscillations from the accretion disk within resonance models if we assume that the central compact object represents a space-time tunnel instead of a Kerr black hole. We have made a systematic study of the existence and stability of time-like circular geodesics in the equatorial plane. As a result, we derived analytical expressions for the epicyclic frequencies that govern the evolution of small deviations from circular motion, which are valid for a general class of traversable space-time tunnels with integrable geodesic equations. We see that for large classes of space-time tunnels, the vertical epicyclic frequency is always positive, which ensures that the circular orbits are always stable with respect to small perturbations in the vertical direction. In this respect, space-time tunnels are similar to a Kerr black hole in that the stability is determined only by the radial epicyclic frequency.

In other respects, the quasi-circular equatorial motion in the space-time of tunnels shows significant differences. A key distinction is that epicyclic and orbital frequencies can obey different types of ordering in different regions of parameter space. Unlike tunnels, for a Kerr black hole they maintain a constant relation for each radius and spin parameter. This property allows the manifestation of a richer class of resonant phenomena in the spacetime of the tunnels, opening up new possibilities to explain the observed quasi-periodic oscillations of the accretion disk. In particular, lower-order parametric and forced resonances are possible, which will lead to stronger observable signals. For a wide range of spin parameters, resonances can be excited in the close vicinity of the tunnel throat, probing the region of strong gravitational interaction.

In addition, the same type of resonance can occur simultaneously at several different radial distances, which may place some constraints on the physical processes in the accretion disc determining the origin of the resonance phenomena.

2 Scalarized black holes in multiscalar Einstein-Gauss-Bonnet gravity

2.1 Multiscalar-Einstein-Gauss-Bonnet gravity

The multiscalar Einstein-Gauss-Bonnet (MSEGB) theory of gravity is defined as follows. We consider a 4-dimensional spacetime $\mathcal{M}$ endowed with a spacetime metric $g_{\mu\nu}$ and N additional scalar fields φ^a that can be considered as coordinates on an N-dimensional Riemannian manifold $\mathcal{E}_N$ (so-called scalar space) with metric $\gamma_{ab}(\varphi)$ [47, 48]. Globally, φ^a is a map $\varphi : \mathcal{M} \to \mathcal{E}_N$ and the kinetic term for the scalar fields given below is exactly the line element of $\mathcal{E}_N$ pulled-back onto spacetime. The action in MSEGB gravity is given by

$$S = \frac{1}{16\pi G}\int d^4x\sqrt{-g}\Big[R - 2g^{\mu\nu}\gamma_{ab}(\varphi)\nabla_\mu\varphi^a\nabla_\nu\varphi^b - V(\varphi) + \lambda^2 f(\varphi)\mathcal{R}^2_{GB}\Big], \tag{19}$$

where R is the Ricci scalar with respect to the space-time metric $g_{\mu\nu}$,$V(\varphi)$ is the potential of the scalar fields $\varphi = (\varphi^1, ..., \varphi^N)$, $f(\varphi)$ is a coupling function depending only on φ, λ is the Gauss-Bonnet coupling constant having dimension *length* and $\mathcal{R}^2_{GB}$ is the Gauss-Bonnet invariant [1].

In the present thesis, we consider the space of scalar fields as a 3-dimensional maximally symmetric Riemannian space, i.e. $\mathbb{S}^3$, $\mathbb{H}^3$ or $\mathbb{R}^3$ with metric

$$\gamma_{ab}(\varphi)d\varphi^a d\varphi^b = a^2\left[d\chi^2 + H^2(\chi)(d\Theta^2 + \sin^2\Theta d\Phi^2)\right], \tag{20}$$

where $a > 0$ is a constant and Θ and Φ are the standard angular coordinates on the 2-dimensional sphere $\mathbb{S}^2$. In addition, we need to define $V(\varphi)$ and the coupling function $f(\varphi)$.

The three space possibilities of the scalar space are given by the metric functions $H(\chi)$:$H(\chi) = \sin\chi$ for spherical geometry, $H(\chi) = \sinh\chi$ for hyperbolic geometry and $H(\chi) = \chi$ for flat geometry. The parameter a is related to the curvature κ of $\mathbb{S}^3$ and $\mathbb{H}^3$, and we have $\kappa = 1/a^2$ for spherical and $\kappa = -1/a^2$ for hyperbolic geometry. In addition, we will consider theories for which the coupling function $f(\varphi)$ and the potential $V(\varphi)$ depend on χ only. This allows the equations for Θ and Φ to be separated from the underlying system.

2.2 Dimensionally reduced equations for scalarized black holes

Instead of making the simplest choice, for which all scalar fields depend only on the radial coordinate r , we choose the nontrivial map $\varphi : \mathcal{M} \to \mathcal{E}_N$ defined as follows. We assume that the field χ depends only on the radial coordinate r, i.e. $\chi = \chi(r)$, and the fields Θ and Φ are independent of r and are given by $\Theta = \theta$ and $\Phi = \phi$ [49]. Our ansatz is compatible with spherical symmetry, and it can be verified that the equations for Θ and Φ are satisfied.

We will consider static and spherically symmetric solutions for black holes of the equations in MSEGB gravity with metric

$$ds^2 = -e^{2\Gamma}dt^2 + e^{2\Lambda}dr^2 + r^2(d\theta^2 + \sin^2\theta d\phi^2), \tag{21}$$

where Γ and Λ depend only on the radial coordinate r.

[1]The Gauss-Bonnet invariant is defined as $\mathcal{R}^2_{GB} = R^2 - 4R_{\mu\nu}R^{\ mu\nu} + R_{\mu\nu\alpha\beta}R^{\mu\nu\alpha\beta}$ where R is the Ricci scalar, $R_{\mu\nu}$ is the tensor of Ricci and $R_{\mu\nu\alpha\beta}$ is the Riemann tensor

For simplicity, in what follows we consider the case with $V(\varphi) = 0$. With the described ansatz for scalar fields and using the form of the metric above, we obtain the following reduced field equations

$$\frac{2}{r}\left[1+\frac{2}{r}(1-3e^{-2\Lambda})\Psi_r\right]\frac{d\Lambda}{dr}+\frac{(e^{2\Lambda}-1)}{r^2}-\frac{4}{r^2}(1-e^{-2\Lambda})\frac{d\Psi_r}{dr} - a^2\left[\left(\frac{d\chi}{dr}\right)^2+2e^{2\Lambda}\frac{H^2(\chi)}{r^2}\right]=0, \tag{22}$$

$$\frac{2}{r}\left[1+\frac{2}{r}(1-3e^{-2\Lambda})\Psi_r\right]\frac{d\Gamma}{dr}-\frac{(e^{2\Lambda}-1)}{r^2} -a^2\left[\left(\frac{d\chi}{dr}\right)^2-2e^{2\Lambda}\frac{H^2(\chi)}{r^2}\right]=0, \tag{23}$$

$$\frac{d^2\Gamma}{dr^2}+\left(\frac{d\Gamma}{dr}+\frac{1}{r}\right)\left(\frac{d\Gamma}{dr}-\frac{d\Lambda}{dr}\right)+\frac{4e^{-2\Lambda}}{r}\left[3\frac{d\Gamma}{dr}\frac{d\Lambda}{dr}-\frac{d^2\Gamma}{dr^2}-\left(\frac{d\Gamma}{dr}\right)^2\right]\Psi_r -\frac{4e^{-2\Lambda}}{r}\frac{d\Gamma}{dr}\frac{d\Psi_r}{dr}+a^2\left(\frac{d\chi}{dr}\right)^2=0, \tag{24}$$

$$\frac{d^2\chi}{dr^2}+\left(\frac{d\Gamma}{dr}-\frac{d\Lambda}{dr}+\frac{2}{r}\right)\frac{d\chi}{dr}-\frac{2\lambda^2}{a^2r^2}\frac{df(\chi)}{d\chi}\left\{(1-e^{-2\Lambda})\left[\frac{d^2\Gamma}{dr^2} +\frac{d\Gamma}{dr}\left(\frac{d\Gamma}{dr}-\frac{d\Lambda}{dr}\right)\right]+2e^{-2\Lambda}\frac{d\Gamma}{dr}\frac{d\Lambda}{dr}\right\}-\frac{2}{r^2}H(\chi)\frac{dH(\chi)}{d\chi}e^{2\Lambda}=0, \tag{25}$$

where

$$\Psi_r=\lambda^2\frac{df(\chi)}{d\chi}\frac{d\chi}{dr}. \tag{26}$$

For this system to describe a black hole the following boundary conditions and regularity conditions must be satisfied. As usual we impose the condition for an asymptotically flat spacetime, namely

$$\Gamma|_{r\to\infty}\to 0,\quad \Lambda|_{r\to\infty}\to 0,\quad \chi|_{r\to\infty}\to 0\ . \tag{27}$$

The very existence of a black hole horizon at $r = r_H$ requires

$$e^{2\Gamma}|_{r\to r_H}\to 0,\quad e^{-2\Lambda}|_{r\to r_H}\to 0. \tag{28}$$

Furthermore, the requirement that the scalar field and its derivatives be regular over the event horizon leads to a set of relations relating the values of the scalar field, its derivatives, and metric functions on the horizon. After suitable manipulations, similar to [50], we can obtain an equation for the first derivative of the scalar field on the horizon $(d\chi/dr)_H$, namely

$$\left(4\lambda^2\left(a^2H(\chi_H)^2-\frac{1}{2}\right)\left(\frac{df(\chi_H)}{d\chi}\right)r_H^3+8H(\chi_H)\left(\frac{dH(\chi_H)}{d\chi}\right)\left(\frac{df(\chi_H)}{d\chi}\right)^2\lambda^4 r_H\right)\left(\frac{d\chi}{dr}\right)_H^2$$
$$+\left(\left(2a^2H(\chi_H)^2-1\right)r_H^4+8H(\chi_H)\left(\frac{dH(\chi_H)}{d\chi}\right)\left(\frac{df(\chi_H)}{d\chi}\right)\lambda^2 r_H^2\right.$$
$$\left.+16\lambda^4a^2\left(a^2H(\chi_H)^2-\frac{1}{2}\right)\left(\frac{df}{d\chi}\right)_H^2H(\chi_H)^2\right)\left(\frac{d\chi}{dr}\right)_H+2H(\chi_H)\left(\frac{dH(\chi_H)}{d\chi}\right)r_H^3$$
$$-\left(\frac{df(\chi_H)}{d\chi}\right)\lambda^2\left(\left(2a^2H(\chi_H)^2-1\right)^2-2\left(2a^2H(\chi_H)^2-1\right)\right)=0 \tag{29}$$

A real root for $(d\chi/dr)_H$ exists if the discriminant is positive, which leads to the following inequality

$$\left(a^2H^2(\chi_H)-\tfrac{1}{2}\right)^2\left(a^4H^4(\chi_H)\left(\tfrac{df}{d\chi}\right)_H^4\lambda^8+\tfrac{3}{2}H(\chi_H)\tfrac{dH(\chi_H)}{d\chi}\left(\tfrac{df}{d\chi}\right)_H^3\lambda^6r_H^2+\right.$$
$$\left.\tfrac{1}{2}\left(a^2H^2(\chi_H)-\tfrac{3}{4}\right)\lambda^4r_H^4\left(\tfrac{df}{d\chi}\right)_H^2+\tfrac{1}{64}r_H^8\right)\geq 0, \tag{30}$$

where the left-hand side in the inequality is the discriminant of the equation (29). Therefore, the inequality serves as a condition for the existence of a black hole, and it turns out that practically for some Gauss–Bonnet coupling functions this introduces a minimum horizon radius below which there are no solutions for black holes. It is easily shown that for a flat scalar space geometry, the inequality reduces to the Gauss-Bonnet black hole existence equation with one scalar field ([50]). The functions Γ and Λ have the usual asymptotics of infinity, and in particular

$$\Lambda\approx\frac{M}{r}+O(1/r^2),\ \ \Gamma\approx-\frac{M}{r}+O(1/r^2), \tag{31}$$

where M is the mass of the black hole. The asymptotic behavior of the scalar field χ can be obtained from the linearized equation for χ away from the black hole, and we find

$$\chi\sim\frac{1}{r^2}. \tag{32}$$

This unusual asymptotics has serious physical implications. This means that the scalar charge associated with χ is zero, which means that the scalar dipole radiation is strongly suppressed. This is very important given the fact that perhaps one of the strongest constraints on gravitational theories with scalar degrees of freedom comes from indirect observations of gravitational wave emission from binary neutron stars [51, 52, 53]. In Gauss-Bonnet theories having a single scalar field it has already been shown that scalarized neutron stars can exist [54] and this is also true for multi-scalar Gauss-Bonnet theories as we will see in the next chapter. The scalar field in neutron stars has the same asymptotics as for the black hole case, meaning that for binary pulsars there is no emission of scalar dipole radiation and no constraints to be placed on the theory based on these observations. This fact shows that the considered theories allow for much wider deviations from GR.

2.3 Numerical formulation and results

The numerical solution of the system of equations (22)–(25) is based on the shooting method with the appropriate boundary conditions at infinity and regularity conditions on the horizon

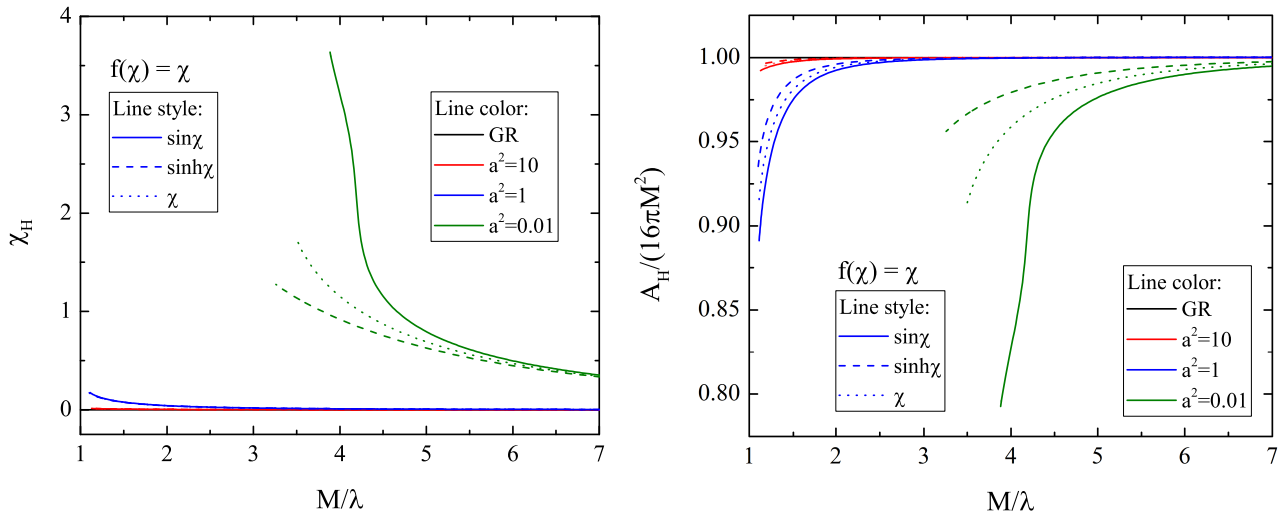

Figure 8: *Left* Value of the scalar field on the horizon as a function of the normalized black hole mass. *Right* Black hole horizon area normalized to the Schwarzschild limit $A_H/(16\pi M^2)$ as a function of normalized mass. The coupling function is $f(\chi) = \chi$ and different colors and line styles correspond to different choices of a^2 and $H(\chi)$ respectively. Sequences of black holes end at the point where the existence condition is violated.

as discussed above. In addition, we also have a condition for the existence of black holes, (30). The calculations were performed using several different forms of the coupling function $f(\chi)$, which admits the existence of black holes with scalar hair, including spontaneously scalarized black holes, for three possible forms of the function $H(\chi)$.

2.3.1 Black holes with scalar hair – linear and exponential coupling

Without loss of generality, we can impose the following condition on the coupling function, namely the condition $f(0) = 0$. This can be done because the field equations are invariant under the transformation $f(\chi) \to f(\chi) + const$. In this subsection, we will discuss the results for two coupling functions representing linear coupling

$$f(\chi) = \chi \tag{33}$$

and an exponential function

$$f(\chi) = e^{\alpha\chi} - 1, \tag{34}$$

where α is a constant. Such a form of the coupling function is also used in Einstein-dilaton-Gauss-Bonnet gravity with a single scalar field [55]. In this case, black hole solutions, when they exist, are always endowed with scalar hair, and the zero scalar field is not a solution to the field equations, unlike the scalarization discussed in the next section.

The two coupling functions are equivalent for small scalar fields χ up to a multiplicative constant. As expected, based on the experience with Einstein-dilaton-Gauss-Bonnet gravity, the qualitative behavior of the solutions is very similar for the two cases - even for large χ and the results are not qualitatively different. Therefore, here we will only present results for linear coupling (33) and where necessary we will comment on the case of exponential coupling (34). The quantities presented above are scaled with respect to the coupling constant λ in the appropriate way, which effectively leaves us with one free parameter in the theory in the case of linear coupling, i.e. a^2 .

The scalar field on the horizon χ_H as a function of the normalized (with respect to λ) black hole mass for linear coupling (33) is presented in the left panel of Figure 9 for different combinations of the parameter a^2 and different functions $H(\chi)$. The scalar field is strong for

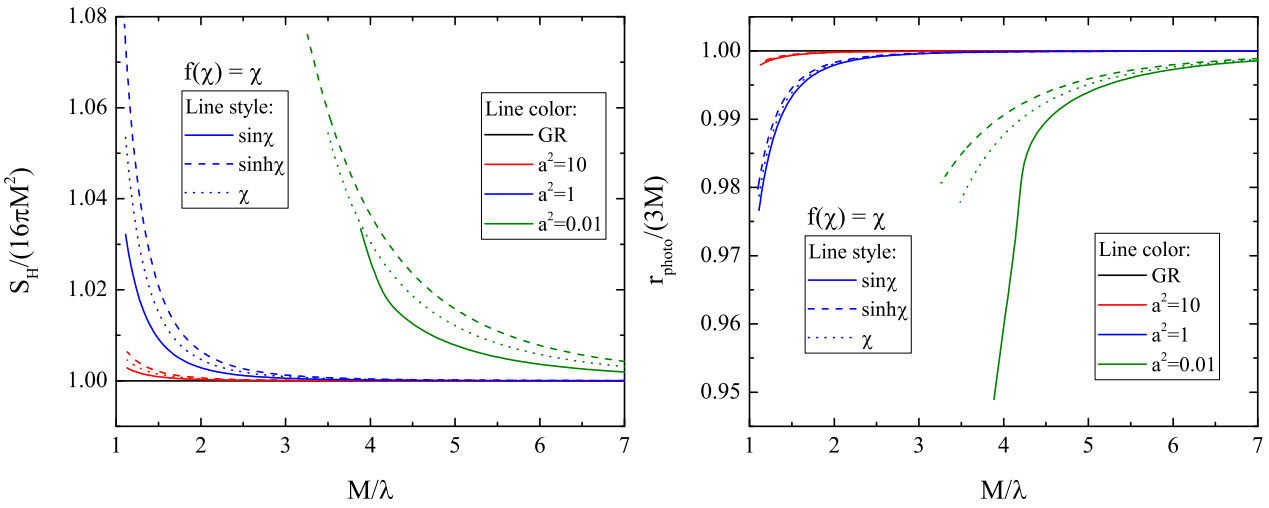

Figure 9: *Left* Schwarzschild limit-normalized black hole entropy $S_H/(16\pi M^2)$ as a function of normalized mass.*Right* Schwarzschild-normalized radius of the photon sphere as a function of normalized mass of the black hole. The coupling function is $f(\chi) = \chi$ and the notation is the same as in Fig. 8

small masses, while for large M it quickly tends to zero. Furthermore, smaller values of a^2 lead to a substantial decrease in χ_H. For fixed a^2, larger values of χ_H are achieved for $H(\chi)$ describing spherical geometry, while the smallest values of χ_H are for hyperbolic geometry. Naturally, larger χ_H will lead to larger differences with GR, and this can be observed in the right panel of Figure 9, where the normalized horizon area is plotted as a function of mass. The normalization of A_H is about the area of the horizon of the Schwarzschild black hole from GR, which corresponds to the horizontal bold line $A_H/(16\pi M^2) = 1$.

Sequences of black hole solutions terminate at some fixed mass where the black hole existence condition (30) is violated and, in general, higher a^2 lead to a smaller limiting mass. For a fixed branch of solutions, the largest deviation is achieved near this limit mass and for the considered range of a^2, the difference with the Schwarzschild horizon area being up to 20% but increasing for smaller a^2. For larger values of M , the black hole branches with a nontrivial scalar field practically merge with the Schwarzschild ones. Numerical studies have been done for a much wider range of a^2 and specifically $a^2 \in [10^{-4}, 10^2]$, and the qualitative behavior remains the same – the Schwarzschild deviations grow (decrease) for smaller (larger) a^2. Our studies show overall that Gauss-Bonnet gravity with a single scalar field and the same coupling function produces a bias that is of the same order as those presented in the figures.

The entropy of a black hole can be calculated using the well-known Wald formula [56],

$$S_H = \frac{1}{4} A_H + 4\pi\lambda^2 f(\chi_H). \tag{35}$$

The entropy normalized to the $4\pi M^2$ Schwarzschild limit is shown in the left panel of Figure 9. It can be seen that a black hole with a scalar hair always has an entropy higher compared to the Schwarzschild one.

Another quantity that is an important characteristic of a black hole is the photon sphere radius $r_{\rm ph}$, defined as the point where the following equality is satisfied

$$\left.\frac{d\Phi}{dr}\right|_{r=r_{\rm ph}} - \frac{1}{r_{\rm ph}} = 0. \tag{36}$$

The photon sphere radius $r_{\rm ph}$ is directly related to many observational properties of black holes such as the frequencies of quasi-normal modes, the black hole shadow, and strong gravitational lensing. The photon sphere radius is presented in the right panel of Figure 9, where

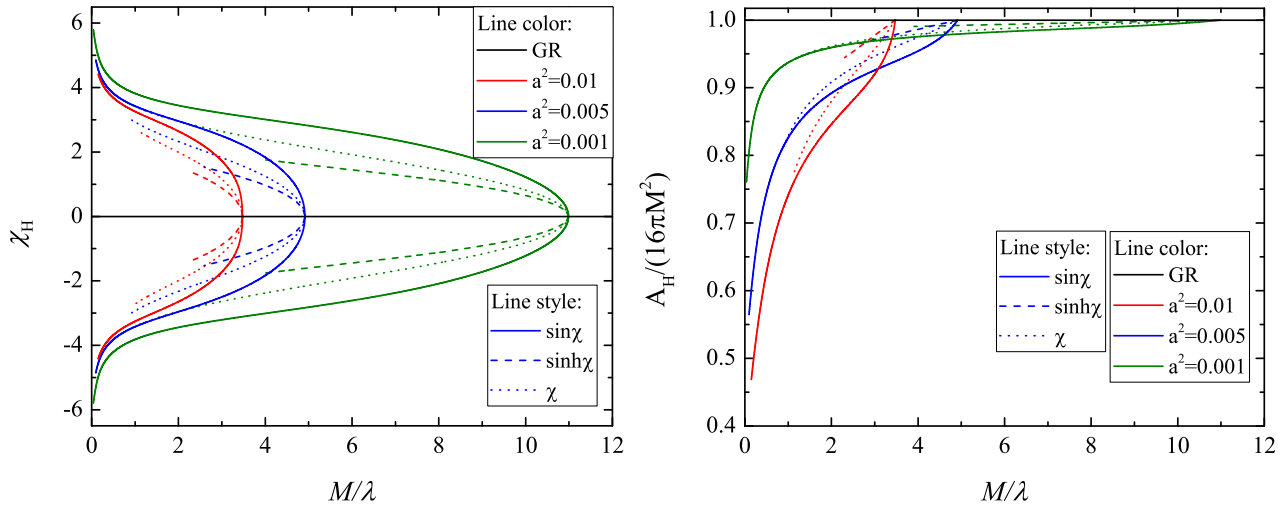

Figure 10: *Left* The value of the scalar field on the horizon as a function of the normalized black hole mass. *Right* The Schwarzschild limit-normalized area of the black hole horizon. The coupling function is $f(\chi) = \frac{1}{2\beta}\left(1 - e^{-\beta\chi^2}\right)$, where $\beta = 0.5$, and the different colors and line styles corresponding to the different choices of a^2 and $H(\chi)$ respectively.

$r_{\rm ph}$ is normalized to the Schwarzschild photon sphere radius. It can be seen that even when the horizon area can differ significantly from the Schwarzschild solution in GR, the deviation in the radius of the photon sphere is quite moderate, roughly around 5%. As we commented, however, smaller values of a^2 will lead to a larger difference with the Schwarzschild solution, and this may cause potential observational effects.

2.3.2 Solutions describing spontaneously scalarized black holes

In this section, we study black hole solutions in multi-scalar Gauss–Bonnet theories, which admit the existence of a solution with zero scalar field (i.e. the Schwarzschild solution) for all values of the parameters. Schwarzschild black holes, however, can become unstable below a certain mass (above a certain curvature of space-time) and spontaneous scalarization can be observed, i.e. new branches of black holes with a non-trivial scalar field bifurcating from those in GR. For spontaneous scalarization to occur, the following conditions must be satisfied

$$\left.\frac{df}{d\chi}\right|_{\chi=0} = 0, \qquad \left.\frac{d^2 f}{d\chi^2}\right|_{\chi=0} > 0. \tag{37}$$

We will discuss two coupling functions satisfying these conditions.

2.3.3 First coupling function

The first coupling function is

$$f(\chi) = \frac{1}{2\beta}\left(1 - e^{-\beta\chi^2}\right), \tag{38}$$

where we fixed $\beta = 0.5$. This is exactly the coupling function used in the beginning to study the spontaneously scalarized Gauss-Bonnet black hole [50] (with one scalar field). This coupling function leads to well-defined branches of scalarized black holes reaching near the $M = 0$ boundary.

The left panel of Figure 10 shows the scalar field on the black hole horizon as a function of the normalized mass for several different values of a^2 and different shapes of the $H(\chi)$ function. The Schwarzschild solution is depicted by the bold black line at $\chi_H = 0$ and it exists for the

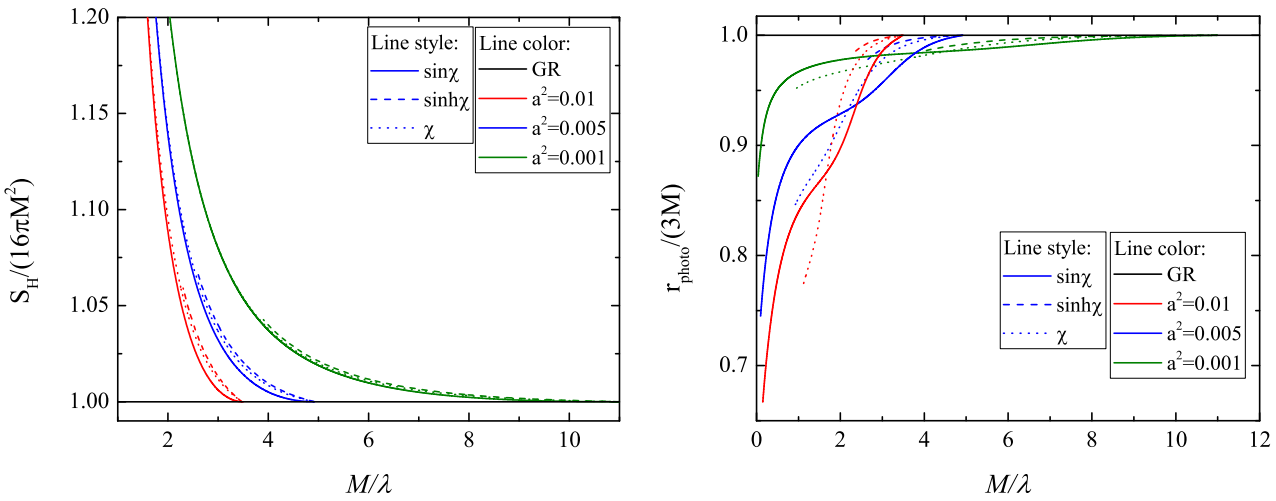

Figure 11: *Left* The Schwarzschild limit-normalized black hole entropy $S_H/(4\pi M^2)$ as a function of normalized mass. *Right* The Schwarzschild-normalized radius of the photon sphere as a function of the normalized black hole mass. The coupling function is $f(\chi) = \chi$ notations are the same as in Figure 10.

entire parameter set. At some values of the mass, however, the Schwarzschild solution becomes unstable and new branches of solutions with a non-trivial scalar field bifurcate from it. It should also be noted that more than one branch of scalarized solutions may exist, and these additional branches can be classified by the number of zeros of the scalar field. Only the first branch that has no nodes of the scalar field can be potentially stable [57, 58] and for that we will focus only on these solutions.

Figure 10 shows that as the parameter a^2 increases, the mass threshold below which scalarization is observed shifts to higher values of M. The deviation of the scalarized black holes from those of the GR can be better seen in the right panel of the figure, where the normalized horizon area is plotted as a function of mass. The differences with GR increase with increasing mass. The solution sequences terminate either because the condition (30) is violated or because of some numerical difficulties – for small masses the equations become very stiff and cannot exceed a certain accuracy. In most cases, however, solutions describing black holes disappear due to violation of the existence condition (30). The situation is similar in pure Gauss-Bonnet gravity with a single scalar field [50]. The main difference between the results for different $H(\chi)$ functions is the mass threshold above which there are no scalarized solutions. The largest differences with GR are observed for hyperbolic geometry of the scalar space.

The next important question is whether the new branches of scalarized solutions are stable or not. Even without dynamic analysis, we can qualitatively predict stability based on thermodynamic considerations alone. A good indicator of the stability of the solutions is the entropy – solutions with greater entropy are thermodynamically favored and are normally the more stable [2]. The normalized entropy is shown in the left panel of Figure 11. As can be seen the Schwarzschild black hole always has a lower entropy than the scalar hair black holes, which gives a strong indication that the scalared solutions are stable. The right panel of Figure 11 shows the radius of the photon sphere. The differences with GR can be significant for small masses and small values of a^2. This could potentially lead to a strong signature of scalar fields in astrophysical observations (quasi-normal modes, gravitational lensing, black hole imaging, etc.). The results so far are for $\beta = 0.5$. Other values of β have been investigated and the results remain qualitatively unchanged. The main difference is the quantitative deviation from GR. More precisely, a smaller β creates larger differences with the Schwarzschild solution for a

[2]Similar conclusions are drawn for pure Gauss-Bonnet gravity with a single scalar field, where stable scalarized solutions also have larger entropy than that of Schwarzschild [50, 57].

fixed black hole mass and a fixed a^2.

2.3.4 Second coupling function

In this subsection, we will focus on a second coupling function that leads to scalarization, namely

$$f(\chi) = \frac{1}{\beta}\left(e^{\beta \sin^2 \chi} - 1\right). \tag{39}$$

The results presented below are for the case $\beta = 1$, but other values of the parameter β are also commented.

The value of the scalar field on the horizon and the normalized horizon area are presented in Figure 12. A very interesting behavior of the scalar branches is observed – after the bifurcation, the mass of the black hole with a scalar hair first increases, then reaches a maximum and decreases. The branches end at $\chi_H \to \pi/2$ because at this point the condition for the existence of scalarized solutions (29) is violated. Then, for a black hole mass between the bifurcation point and the mass maximum for the scalarized branch, there exist three black hole solutions – the Schwarzschild solution itself and two scalarized solutions. Similar behavior was first observed for scalar charged black holes with nonlinear electrodynamics [59, 60] and recently also for a Gauss-Bonnet black hole with a single scalar field [61], where the coupling function is a coupling function with a term of 4th order. The results presented here, however, clearly show the emergence of a small region where two scalarized solutions with the same mass coexist, and the most important question we have to ask is about their stability. As we commented in the previous subsections, studying the black hole entropy (35) can provide information about the stability of branches. The normalized entropy is presented in the left panel of Figure 13 as a function of mass. For small masses, the scalarized branches have an entropy larger than the Schwarzschild one, and on this basis we expect that the three solutions (for the three different $H(\chi)$ functions) are stable. As the mass of the scalarized branches increases, they reach a maximum where a cusp appears on the $S_H(M)$-diagram, which is a signal of a change in stability. From this point on, the scalarized branch is most likely unstable, since its entropy is lower than that in GR. This matches what is observed for charged scalarized blacks holes in [59]. There is also another interesting region near the mass maximum where the potentially stable part of the scalarized branch has for a small range of masses a lower entropy than that of Schwarzschild. Furthermore, the Schwarzschild solution is most likely stable everywhere along the path to the bifurcation point. This is a very interesting region and the question of stability can only be rigorously answered if a linear stability analysis is done. It will be done in a future paper.

The normalized radius is plotted in the right panel of Figure 11. The Schwarzschild difference is expectedly larger for smaller masses and reaches up to 10%. This will of course depend on the choice of the parameters β and a^2. If we assume that the middle of the branch (between the bifurcation point and the mass maximum) is truly unstable, there will clearly be a jump between the last stable Schwarzschild model and the stable scalarized black hole of the same mass. This could potentially lead to interesting observational effects in scenarios involving a scalarization process, such as in merging compact objects [62, 63, 64].

It is interesting whether such strange behavior can be observed in pure Gauss-Bonnet gravity with a single scalar field. Our results show that for the coupling function (39) and properly chosen values of β , the mass of scalarized black holes starts to increase after the bifurcation point, but the corresponding condition for the existence of scalarized black holes ((30) is quickly violated and branches terminate before a clear mass maximum is reached. Of course, careful tuning of the parameter β and/or the coupling function can lead to the desired effect, moreover such behavior (but not so pronounced) has already been observed for a coupling function with a quartic term in the scalar field [61]. At the end of the section, let us comment on the

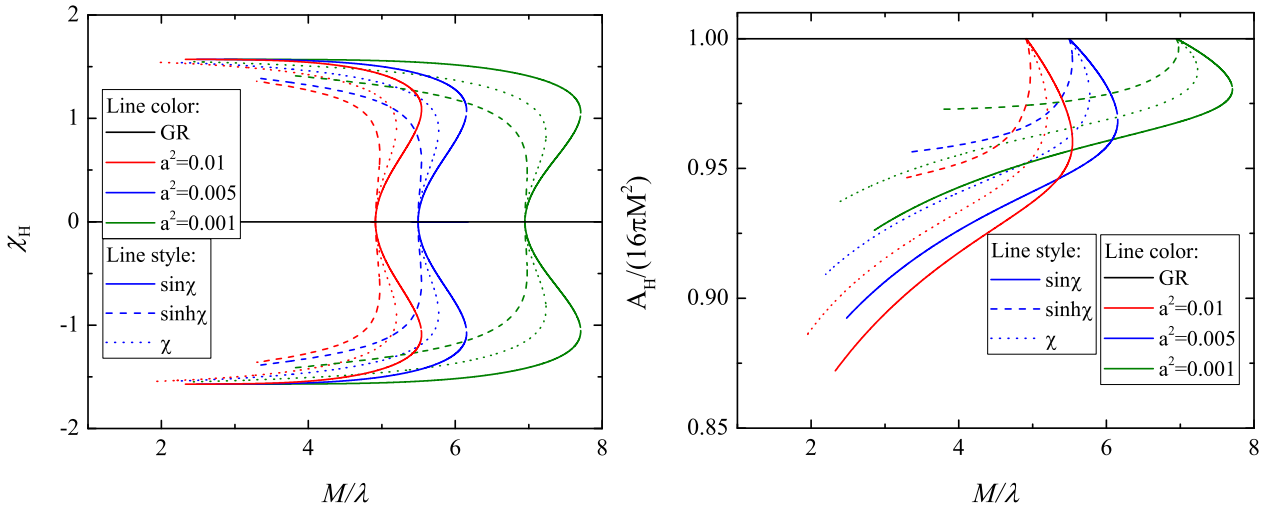

Figure 12: *Left* The value of the scalar field on the horizon as a function of the normalized black hole mass. *Right* The normalized area of the black hole horizon, to the Schwarzschild limit $A_H/(16\pi M^2)$, as a function of mass. The coupling function is $f(\chi) = (1/\beta)(e^{\beta \sin^2 \chi} - 1)$ where $\beta = 1$, and the different line colors and styles correspond of different choices of a^2 and $H(\chi)$ respectively.

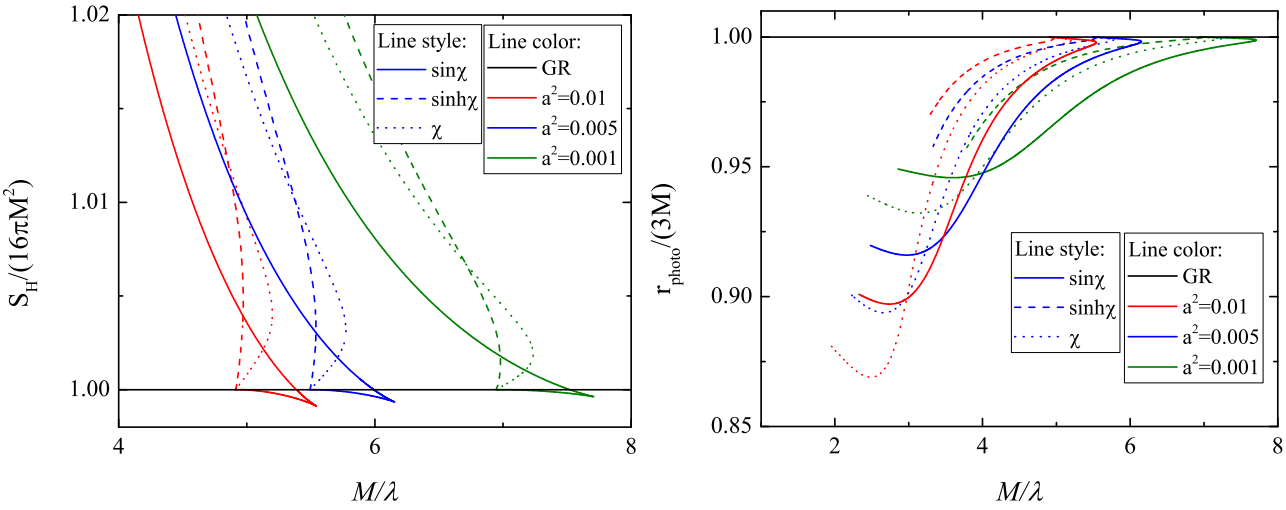

Figure 13: *Left* The Schwarzschild limit normalized black hole entropy $S_H/(4\pi M^2)$ as a function of normalized mass. *Right* The Schwarzschild-normalized radius of the photon sphere as a function of black hole mass. The coupling function is $f(\chi) = (1/\beta)(e^{\beta \sin^2 \chi} - 1)$ where $\beta = 1$ and the notation is the same as in Figure 12.

dependence of the results on the parameter β in the coupling function (39). It turns out that the interesting behavior we observed above disappears for sufficiently small β , while for large β the range of masses between the bifurcation point and the maximum mass for the scalarized solutions increases. In the case that the nonuniqueness of the scalarized branch vanishes, the behavior of the solutions is qualitatively the same as for the coupling function (38) and therefore we will not comment on it further.

2.4 Conclusion

In this chapter, we considered a multiscalar extension of GR, namely Gauss-Bonnet gravity, and focused on models whose scalar space $\mathcal{E}_N$ is a 3-dimensional maximally symmetric space, i.e. $\mathbb{S}^3$, $\mathbb{H}^3$ or $\mathbb{R}^3$. We restricted ourselves to the static and spherically symmetric case with a map $\varphi : \mathcal{M} \to \mathcal{E}_3$ explicitly given by $\varphi = (\chi(r), \Theta = \theta, \Phi = \phi)$ which is compatible with spherical symmetry. Assuming also that the coupling function depends only on χ we numerically prove the existence of black holes in multi-scalar-Einstein-Gauss-Bonnet theories. An important property for these solutions is that the scalar field has $1/r^2$ asymptotics at infinity, leading to zero scalar charge and negligible dipole radiation. Thus, we cannot place strict observational constraints on the parameters based on the indirect observation of gravitational waves from pulsars in binary systems.

We concentrated on different coupling functions leading to black holes with a scalar hair. For all cases of scalar hair black holes studied, we find that in the limit $a^2 \to \infty$ the results approach those in GR, and the highest deviations are observed for small values of a^2. However, there exists a finite mass below which no black hole solutions exist, which depends on the parameter a^2 and increases as a^2 decreases. Regarding the dependence of the results on the $H(\chi)$ function, the highest deviation from GR is observed for a spherical geometry and the least for a hyperbolic one. Spontaneously scalarized black holes have standard characteristics – at some masses, new classes of solutions with a non-trivial scalar field bifurcate from the Schwarzschild one. The bifurcation point moves to smaller masses with an increment of a^2. The deviations from GR are strongly dependent on the choice of parameters, and larger deviations are observed for smaller a. The branches either reach zero mass, leading to a strong growth of the scalar field and larger Schwarzschild differences for small M , or end up at some finite mass due to violation of the black hole existence condition. For one of these coupling functions that we have considered, a very interesting phenomenon is observed – the scalarized branch first moves to larger masses and then reaches a maximum for M , the mass starts to decrease. Thus two sub-branches can be distinguished – middle, between the bifurcation point and maximum mass, and an outer branch after the maximum mass. Based on thermodynamic studies, we can conclude that most likely the middle branch is unstable, while the outer branch is stable.

If we assume that the approximate thermodynamic stability analysis coincides with an as yet unexplored linear stability of the solutions, then there will be interesting consequences, especially for phenomena involving the dynamical scalarization of black holes. The reason is that we will not have a smooth transition between scalarized and unscalarized solutions, as is the standard case where the scalarized branches are potentially stable just from the bifurcation point where the scalar field tends to zero. In contrast, we will have a jump between the last Schwarzschild black hole and a stable scalarized black hole branch. Furthermore, there may be a region in the parameter space where stable Schwarzschild black holes coexist with stable scalarized black holes. As a result, a jump can be observed between the scalarized and non-scalarized solutions. For example, this could manifest as a sudden change in gravitational wave frequencies during a collision.

We also investigated the space-time surrounding the resulting black hole solutions and more specifically the photon sphere radius, which is directly related to various astrophysical manifestations of black holes. In all cases, we found that the deviations from GR are more significant

for smaller black hole masses. For the studied coupling function shapes and parameter values, the largest differences with the Schwarzschild black hole are reached for the scalarized solution with a maximum deviation of approximately 30%. This value would potentially increase if we consider smaller a^2.

3 Neutron stars in the Gauss-Bonnet multiscalar theory

3.1 Dimensionally reduced equations for scalarized neutron stars

Here we will consider only the static and spherically symmetric solutions for neutron stars satisfying the MSEGB gravity equations with metric

$$ds^2 = -e^{2\Gamma}dt^2 + e^{2\Lambda}dr^2 + r^2(d\theta^2 + \sin^2\theta d\phi^2), \tag{40}$$

where Γ and Λ depend only on the radial coordinate r.

The geometric formulation fully follows the formulation for black holes with the same ansatz for the scalar fields. In this way, we obtain the following reduced field equations:

$$\frac{2}{r}\left[1+\frac{2}{r}(1-3e^{-2\Lambda})\Psi_r\right]\frac{d\Lambda}{dr} + \frac{(e^{2\Lambda}-1)}{r^2} - \frac{4}{r^2}(1-e^{-2\Lambda})\frac{d\Psi_r}{dr} - a^2\left[\left(\frac{d\chi}{dr}\right)^2 + 2e^{2\Lambda}\frac{H^2(\chi)}{r^2}\right] = 8\pi\rho e^{2\Lambda}, \tag{41}$$

$$\frac{2}{r}\left[1+\frac{2}{r}(1-3e^{-2\Lambda})\Psi_r\right]\frac{d\Gamma}{dr} - \frac{(e^{2\Lambda}-1)}{r^2} - a^2\left[\left(\frac{d\chi}{dr}\right)^2 - 2e^{2\Lambda}\frac{H^2(\chi)}{r^2}\right] = 8\pi p e^{2\Lambda}, \tag{42}$$

$$\frac{d^2\Gamma}{dr^2} + \left(\frac{d\Gamma}{dr}+\frac{1}{r}\right)\left(\frac{d\Gamma}{dr}-\frac{d\Lambda}{dr}\right) + \frac{4e^{-2\Lambda}}{r}\left[3\frac{d\Gamma}{dr}\frac{d\Lambda}{dr} - \frac{d^2\Gamma}{dr^2} - \left(\frac{d\Gamma}{dr}\right)^2\right]\Psi_r - \frac{4e^{-2\Lambda}}{r}\frac{d\Gamma}{dr}\frac{d\Psi_r}{dr} + a^2\left(\frac{d\chi}{dr}\right)^2 = 8\pi p e^{2\Lambda}, \tag{43}$$

$$\frac{d^2\chi}{dr^2} + \left(\frac{d\Gamma}{dr} - \frac{d\Lambda}{dr} + \frac{2}{r}\right)\frac{d\chi}{dr} - \frac{2\lambda^2}{a^2r^2}\frac{df(\chi)}{d\chi}\left\{(1-e^{-2\Lambda})\left[\frac{d^2\Gamma}{dr^2} + \frac{d\Gamma}{dr}\left(\frac{d\Gamma}{dr}-\frac{d\Lambda}{dr}\right)\right] + 2e^{-2\Lambda}\frac{d\Gamma}{dr}\frac{d\Lambda}{dr}\right\} = \frac{2}{r^2}H(\chi)\frac{dH(\chi)}{d\chi}e^{2\Lambda}, \tag{44}$$

where

$$\Psi_r = \lambda^2\frac{df(\chi)}{d\chi}\frac{d\chi}{dr}, \tag{45}$$

a ρ and p are the energy density and matter pressure in the neutron star.

We must supplement the above dimensionally reduced field equations with the hydrostatic equation of the fluid:

$$\frac{dp}{dr} = -(\rho+p)\frac{d\Gamma}{dr}. \tag{46}$$

3.2 Numerical formulation and results

In the present paper, we present results for a realistic equation of state (EOS) called MPA1 [65]. This EOS allows for maximum neutron star masses greater than 2 solar masses, and it is in agreement with the constraints set by observations of merging neutron star binaries [66]. For numerical calculations, we adopt its polytropic approximation [67]. We will consider various coupling functions $f(\chi)$ that admit spontaneous scalarization, i.e. satisfy the condition $\frac{df}{d\chi}(0) = 0$. As an example, we will consider the following coupling function

$$f(\chi) = -\frac{1}{2\beta}\left(1 - e^{-\beta\chi^2}\right), \tag{47}$$

where β is a positive parameter. The coupling constant λ is represented in dimensionless units

$$\lambda \to \frac{\lambda}{R_0}, \tag{48}$$

where $R_0 = 1.476$ km is half of the gravitational radius of the Sun.

Numerically finding the scalarized solutions and computing the scalarized branches is a difficult and time-consuming process. That is why we will limit ourselves to only one EOS and one coupling function, and our main task is to construct representative solutions and determine their main properties and dependence on the parameters of the theory. The reduced field equations (41)-(44) and the hydrostatic equilibrium equations (46) are solved numerically with the natural boundary conditions - regularity at the center of the star and asymptotically flat at infinity :

$$\Lambda(0) = 0, \quad \frac{d\Gamma}{dr}(0) = 0, \quad \chi(0) = 0, \tag{49}$$

and

$$\Lambda|_{r\to\infty} \to 0, \quad \Gamma|_{r\to\infty} \to 0, \quad \chi|_{r\to\infty} \to 0. \tag{50}$$

The asymptotic behavior of the scalar field, as in the case of black holes, can be obtained by linearizing the field equations in the asymptotic region, which gives $\chi \sim 1/r^2$. This asymptotics shows that the scalar field does not possess a scalar charge. This has important physical implications for the theory. The absence of scalar charge means that dipole scalar radiation in the binary system will be strongly suppressed, so there are no strong constraints that can be placed on the parameters of the theory from observations of binary pulsars.

For the coupling function we use, the trivial scalar field $\chi = 0$ is always a solution to the field equations (41)-(44) and the results match those of general relativity. From now on, trivial solutions and GR solutions will be used interchangeably. We will search the three-dimensional parameter space (a^2, λ, β) for bifurcation points from which new solution branches with a nontrivial scalar field emerge from the trivial branch. This task turned out to be non-trivial. On the one hand is the number of free parameters in the theory, and on the other - the serious numerical difficulties arising from the system itself (41)-(44).

As for the different scalar spaces, we found solutions for all three. However, the differences between them are negligibly small and cannot be seen when comparing the results in the figures. We explain the lack of deviations with the small values of the scalar field. We found that even for the maximum observed values of the scalar fields, the values of the metric functions $H(\chi) = \sin(\chi)$, $H(\chi) = \chi$ and $H(\chi) = sinh(\chi)$ are practically indistinguishable. We therefore chose to present only the results for the spherical scalar space with $H(\chi) = \sin(\chi)$.

In Fig. 14 we plot the star's mass, in solar masses, as a function of its radius in km. In the left panel, the value of a^2 is fixed and different combinations of λ and β are studied. In the right panel, λ and β are fixed and different values of a^2 are studied. It is clear from both panels that the results are qualitatively similar to the results in pure Gauss–Bonnet gravity presented in

[68]. Non-trivial solutions emerge from the bifurcation points and the branches terminate either after reaching a maximum mass or at some smaller mass due to numerical difficulties. For all parameter sets, the computational procedure becomes more sensitive to the initial conditions as the central energy density increases, and the computational time for the individual models increases continuously along the branch. Therefore, some of the branches were terminated before the maximum mass, in some reasonable computational time. Maximum mass, when reached, is always lower than GR. However, we found that for the same set of parameters, λ and β, a value for a^2 (less than one) can be chosen such that the GBT and MSAGBT solutions bifurcate for one and same central density. In this case, MSEGBT neutron stars have a smaller mass compared to GB theory with a single scalar field.

In the left panel of the figure, it can be seen that for a fixed value of a^2 the bifurcation point moves to higher masses (equivalently – central densities) with decreasing λ. With λ fixed, the branch of the non-trivial solution becomes longer and tends to GR as β increases (the bifurcation point does not move). In the limiting case $\beta \to \infty$ the non-trivial branch will coincide with the trivial one. In the right panel, it can be seen that with fixed λ and β the bifurcation point moves to higher masses and the branch becomes longer as a^2 increases.

The behavior described above may place some constraints on the free parameters in the theory. If the equation of state allows for maximum masses higher than two solar masses in the GR, the theory parameters must be chosen in such a way that the maximum mass is above two solar masses. However, this is not very restrictive, since two of the parameters allow significant deviations in the bifurcation point, and the $\beta \to \infty$ case always tends to the trivial solution, no matter what the values of the other two parameters are. Also, not all branches reach maximum masses.

For all parameter combinations presented, we were able to find branches of solutions with different numbers of zeros of the scalar field – no zeros, one zero, etc. We find that the bifurcation point moves to higher masses and the branch becomes shorter as the number of field zeros increases. The results presented here are only for solutions without zeros. These solutions, as explained below, are stable.

In Fig. 15 we plot the neutron star mass as a function of central density. The models presented in the left and right panels correspond to those in Fig. 14. For all models, the deviations from GR are relatively small.

Due to the absence of scalar charge, in Fig. 16 we plotted the value of the surface scalar field χ_S of the star as a function of the mass of the neutron star. χ_S is always higher for smaller values of λ and decreases as β increases. At the same time, a^2 has no significant effect on the maximum value of χ_S.

As an indication of the stability of the neutron star solutions, in Fig. 17 we present the binding energy of the star, $1-\frac{M_0}{M_{\rm sun}}$, as a function of $M_0/M_{\rm sun}$, where M_0 is the baryonic mass of the star. For better visualization, only some of the parameters discussed above are presented. Solutions in MSEGBT have a higher (in absolute value) binding energy compared to GR, making them energetically more favoured. The peak in the GR solution marks the unstable patterns in the mass-density dependence.In the case of MSEGBT, such a threshold is also present for the sets of parameters for which the maximum mass can be reached. Models with zeros of the scalar field have lower (in absolute value) binding energy than the corresponding ones without zeros. Therefore, by analogy with other scalar-tensor thories, solutions with zeros of the scalar field are unstable.

4 Conclusion

In this chapter, we constructed scalarized neutron stars in multiscalar Gauss-Bonnet theory with a maximally symmetric scalar space and a nontrivial map $\varphi : spacetime \to targer\ space$

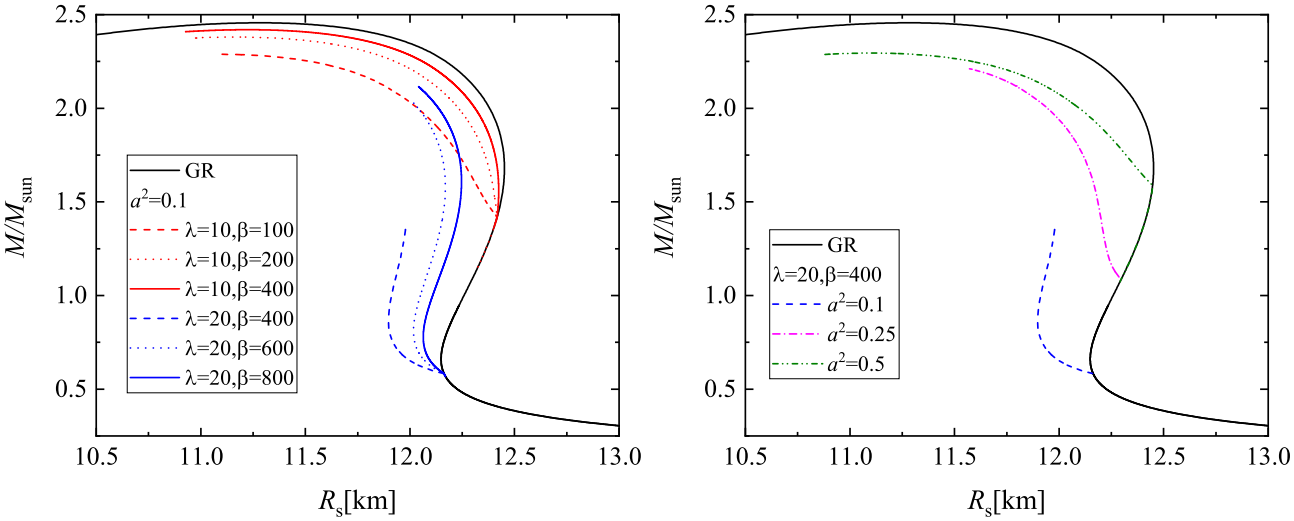

Figure 14: The mass-radius relation for models with different parameter values. *Left* Fixed value of a^2 and different values of λ and β. *Right* Fixed value of λ and β and different values of a^2. The mass of the star is in solar masses and the radius is in kilometers.

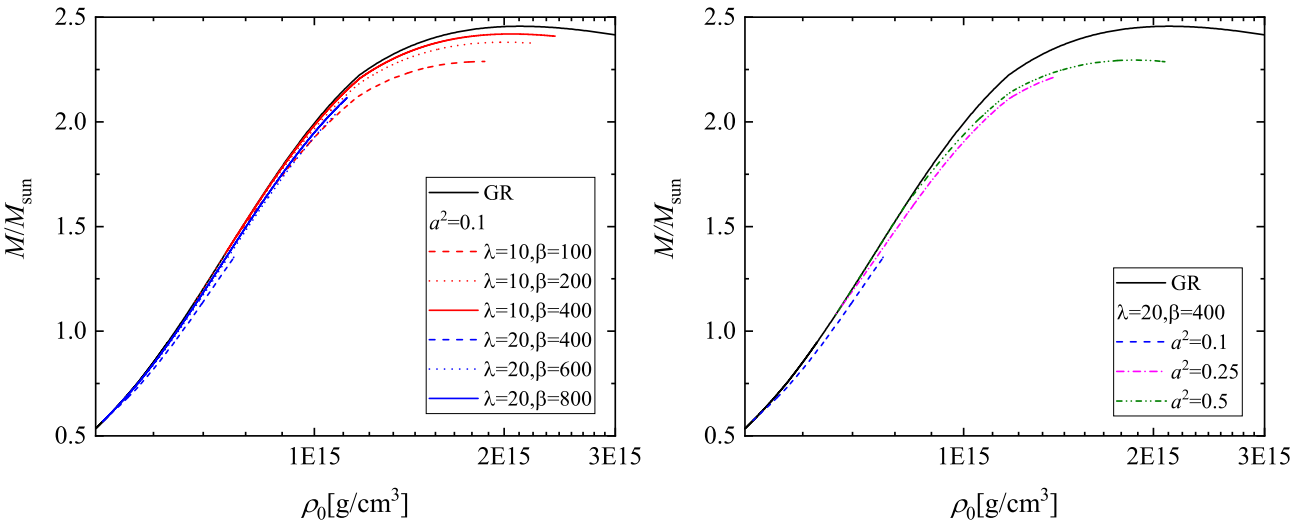

Figure 15: The stellar mass as a function of central density for models with different parameter values. *Left* Fixed value for a^2 and different values for λ and β. *Right* Fixed value for λ and β and different values for a^2. The mass of the star is in solar masses and the energy density in – g/cm^3.

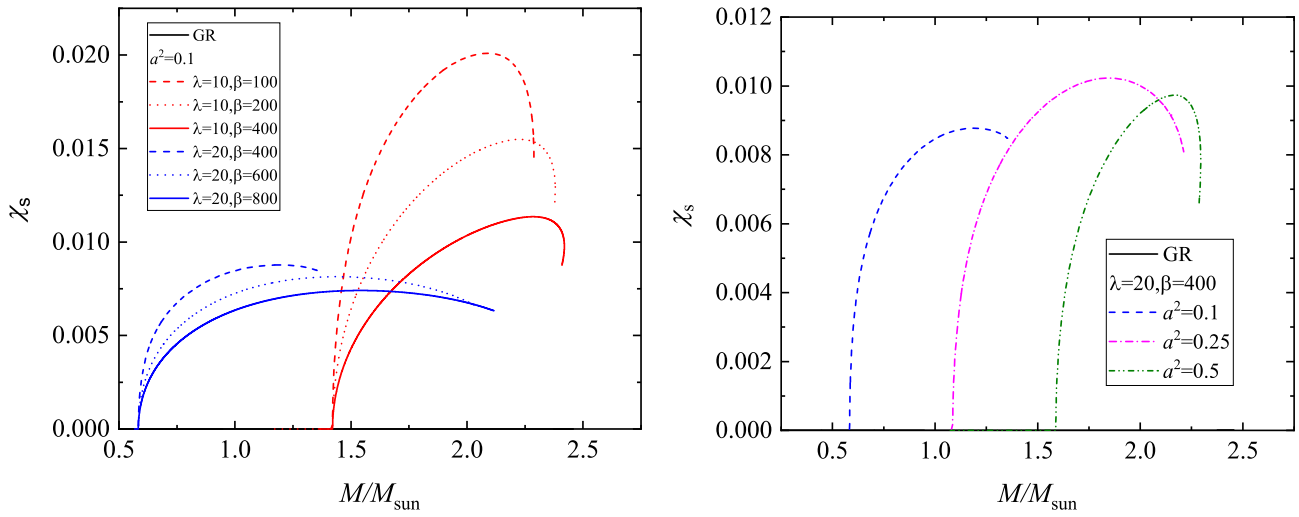

Figure 16: The value of the scalar field on the surface of the star as a function of the star's mass. *Left* Fixed value for a^2 and different values for λ and β. *Right* Fixed value for λ and β and different values for a^2. The star's mass is in solar masses.

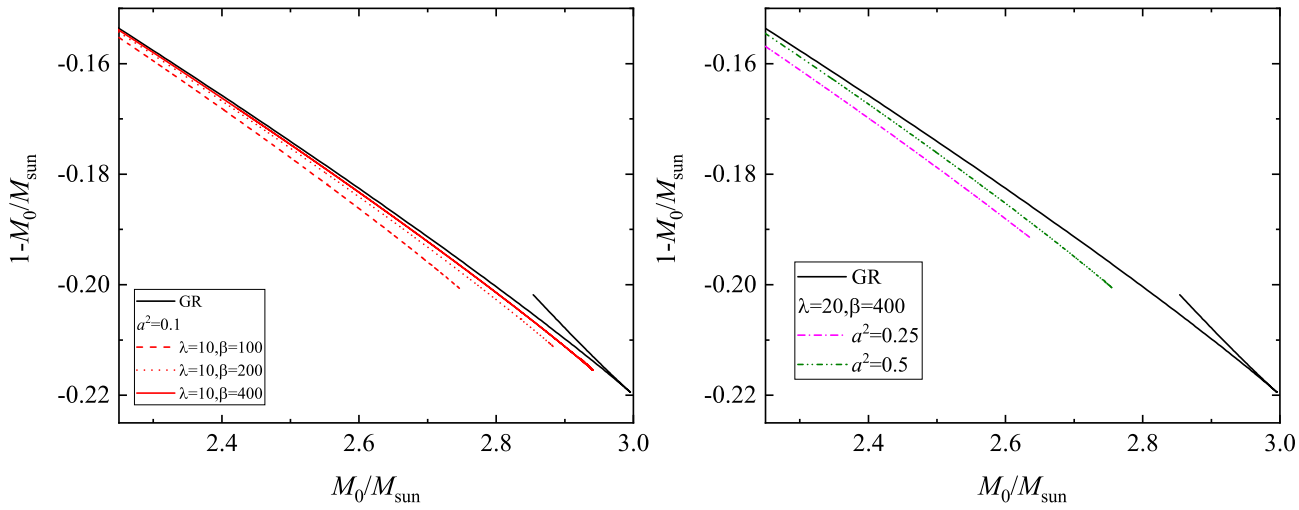

Figure 17: The binding energy $1 - M_0/M_{\rm sun}$ as a function of the rest mass of the star M_0. *Left* Fixed value for a^2 and different values for λ and β. *Right* Fixed value for λ and β and different values for a^2. The rest mass of the star is in solar masses.

compatible with spherical symmetry and explicitly given by $\varphi = (\chi(r), \Theta = \theta, \Phi = \phi)$. We explored the simplest three possible choices for a maximally symmetric scalar space, namely $\mathbb{S}^3$, $\mathbb{H}^3$, and $\mathbb{R}^3$. The models we investigated have a zero scalar field at the center of the star, and the results presented are for a coupling function that allows scalarization. In terms of scalar space, no differences are observed between the solutions in the three cases. This is easily explained by the low values of the scalar field, which makes the metric function $H(\chi)$ that defines the target space effectively indistinguishable between the three cases. Therefore, the presented results are only for scalar space with spherical geometry.

The resulting neutron star solutions appear qualitatively similar to neutron star solutions in pure GB gravity. Branches with a non-trivial scalar field branch off from the trivial solution, and the maximum mass of the scalarized solutions is always less than that in GR. For the same sets of values for the parameters in the theory, there exist multiple solution branches characterized by the number of zeros the scalar field has. However, the bifurcation point depends strongly on the value of the coupling constant λ, the parameter a^2 in the scalar space metric, and the number of zeros of the scalar field. The maximum mass of the solutions in MSEGBT is always lower compared to GR, which may allow imposing some constraints on the theory parameters. At the same time, however, due to numerical difficulties, not all decision branches reach maximum mass.

To get some indication of the stability of the scalarized models, we investigated the binding energy of the $1 - M_0/M_{sun}$ star. Scalarized solutions have a higher (in absolute value) binding energy than GR, making them energetically favored. As for the branches with different number of zeros of the scalar field, the branch without zeros has the highest (in absolute value) binding energy, therefore this branch is stable and the other branches are unstable. This conclusion is based on the binding energy and behavior of neutron star solutions in similar theories. However, for a definitive answer on the stability of the models, the radial perturbations must be investigated.

Dissertation Contributions

• The quasi-periodic oscillations of the accretion disk around rotating traversable space tunnels are investigated using the resonance models. The linear stability of circular geodesic orbits in the equatorial plane for a general class of space tunnel geometries is also investigated and analytical expressions for epicyclic frequencies are derived. Since space tunnels can often mimic black holes in astrophysical observations, we analyze the properties of quasi-circular oscillating motions compared to a Kerr black hole. We show that space tunnels possess distinctive features that may be important for observations. A characteristic of Kerr black holes is that the orbital and epicyclic frequencies obey a constant ordering over the entire range of the spin parameter. In contrast, in tunnels we can have different types of orderings between frequencies in different regions of the parameter space. This allows the excitation of many more diverse types of resonances, including lower-order parametric and forced resonances, which can lead to stronger visible signals. In addition, for uniformly rotating orbits, resonances can be excited in the very close vicinity of the tunnel throat for a wide range of angular momentum values, making tunnels a valuable laboratory for testing strong gravity.

• The existence of black holes in multiscalar Gauss-Bonnet theories with a maximally symmetric scalar space for several coupling functions, including the case of spontaneous scalarization, is numerically proven. Various characteristics of black holes and the space-time around them, such as the horizon area, entropy and radius of the photon sphere, have also been systematically investigated. One of the most important properties of the resulting solutions is that the scalar charge is zero and thus the scalar dipole emission is suppressed, leading to much weaker observational constraints on the theory. For one of the coupling functions, we find branches of scalarized black holes that have a non-trivial structure - there is a non-uniqueness of the scalarized solutions.

• Solutions describing spontaneously scalarized neutron stars in Gauss-Bonnet multiscalar theories with maximally symmetric scalar space are numerically constructed. The dependences $M(\rho)$ and $M(R)$ were constructed, as well as the dependence of the binding energy on the baryon mass, which also carry information about the stability of the neutron stars.

Publications in refereed journals included in the dissertation

Publications in international refereed journals

A1. Efthimia Deligianni, Jutta Kunz, Petya Nedkova, Stoytcho Yazadjiev, and Radostina Zheleva, Quasiperiodic oscillations around rotating traversable wormholes, Phys. Rev. D 104, 024048 – Published 19 July 2021.

A2. Daniela D. Doneva, Kalin V. Staykov, Stoytcho S. Yazadjiev, and Radostina Z. Zheleva, Multiscalar Gauss-Bonnet gravity: Hairy black holes and scalarization, Phys. Rev. D 102, 064042 – Published 15 September 2020.

A3. Staykov, K.V., Zheleva, R.Z., Scalarized non-topological neutron stars in multi-scalar Gauss-Bonnet gravity, Eur. Phys. J. C 82, 108 (2022) – Published 04 February 2022.

Acknowledgments

I would like to thank my scientific supervisor, Prof. Stoytcho Yazadjiev for the opportunity to work in this field of theoretical physics and in his highly qualified scientific group.

I thank my colleagues Dr. Kalin Staykov and Dr. Petya Nedkova for our joint work.

I express my great gratitude and appreciation to my colleague Assoc. Prof. Galin Gyulchev for his indispensable help in the writing and technical layout of the dissertation, as well as his help during all my years of study in the Gravity group and his moral support.

I thank Assoc. Prof. Dimitar Mladenov for his great help in all kinds of questions and in all kinds of situations during all my years of study. I wouldn't have gotten here without his help. I was lucky to come across such a conscientious and responsible person who is always ready to help in any way he can.

I thank all my teachers from the Department of Theoretical Physics for their efforts in my studies.

I thank Sofia Iskrenova and Lidiya Slavova for their cooperation and help with administrative issues and documents.

References

[1] M. Feroci and al. The LOFT mission concept: a status update. In Jan-Willem A. den Herder, Tadayuki Takahashi, and Marshall Bautz, editors, *SPIE Proceedings*. SPIE, jul 2016.

[2] S. N. Zhang and al. eXTP: Enhanced x-ray timing and polarization mission. In Jan-Willem A. den Herder, Tadayuki Takahashi, and Marshall Bautz, editors, *SPIE Proceedings*. SPIE, jul 2016.

[3] Wilson-Hodge and al. STROBE-X: X-ray timing and spectroscopy on dynamical timescales from microseconds to years. January 2017.

[4] Dimitrios Psaltis, Tomaso Belloni, and Michiel van der Klis. Correlations in quasi-periodic oscillation and noise frequencies among neutron star and black hole x-ray binaries. *The Astrophysical Journal*, 520(1):262–270, jul 1999.

[5] Christopher W. Mauche. Correlation of the quasi-periodic oscillation frequencies of white dwarf, neutron star, and black hole binaries. *The Astrophysical Journal*, 580(1):423–428, nov 2002.

[6] Shoji Kato and al. *Trapped Radial Oscillations of Gaseous Disks around a Black Hole*. Publications-Astronomical Society of Japan, 1980.

[7] Shoji Kato. Resonant excitation of disk oscillations by warps: A model of kHz QPOs. *Publications of the Astronomical Society of Japan*, 56(5):905–922, oct 2004.

[8] L. Rezzolla, S'i. Yoshida, T. J. Maccarone, and O. Zanotti. A new simple model for high-frequency quasi-periodic oscillations in black hole candidates. *Monthly Notices of the Royal Astronomical Society*, 344(3):L37–L41, sep 2003.

[9] M. A. Abramowicz and W. Kluźniak. A precise determination of black hole spin in GRO j1655-40. *Astronomy and Astrophysics*, 374(3):L19–L20, aug 2001.

[10] Marek A. Abramowicz, Vladimir Karas, Wodzimierz Kluźniak, William H. Lee, and Paola Rebusco. Non-linear resonance in nearly geodesic motion in low-mass x-ray binaries. *Publications of the Astronomical Society of Japan*, 55(2):467–471, apr 2003.

[11] W. Kluźniak and M. A. Abramowicz. Resonant oscillations of accretion flow and khz QPOS. *Astrophysics and Space Science*, 300(1-3):143–148, nov 2005.

[12] G. Török, M. A. Abramowicz, W. Kluźniak, and Z. Stuchlík. The orbital resonance model for twin peak kHz quasi periodic oscillations in microquasars. *Astronomy and Astrophysics*, 436(1):1–8, may 2005.

[13] Luigi Stella and Mario Vietri. kHz quasiperiodic oscillations in low-mass x-ray binaries as probes of general relativity in the strong-field regime. *Physical Review Letters*, 82(1):17–20, jan 1999.

[14] Zdeněk Stuchlík and Andrea Kotrlová. Orbital resonances in discs around braneworld kerr black holes. *General Relativity and Gravitation*, 41(6):1305–1343, nov 2008.

[15] Alikram N Aliev, Göksel Daylan Esmer, and Pamir Talazan. Strong gravity effects of rotating black holes: quasi-periodic oscillations. *Classical and Quantum Gravity*, 30(4):045010, jan 2013.

[16] Tim Johannsen and Dimitrios Psaltis. Testing the no-hair theorem with observations in the electromagnetic spectrum. iii. quasi-periodic variability. *The Astrophysical Journal*, 726(1):11, dec 2010.

[17] Andrea Maselli, Leonardo Gualtieri, Paolo Pani, Luigi Stella, and Valeria Ferrari. Testing gravity with quasi-periodic oscillations from accreting black holes: the case of the Einstein-Dilaton-Gauss-Bonnet theory. *The Astrophysical Journal*, 801(2):115, mar 2015.

[18] F H Vincent. Testing chern–simons gravity with black holes? *Classical and Quantum Gravity*, 31(2):025010, dec 2013.

[19] Andrea Maselli, Paolo Pani, Leonardo Gualtieri, and Valeria Ferrari. Rotating black holes in einstein-dilaton-gauss-bonnet gravity with finite coupling. *Physical Review D*, 92(8):083014, oct 2015.

[20] Andrea Maselli, Paolo Pani, Roberto Cotesta, Leonardo Gualtieri, Valeria Ferrari, and Luigi Stella. Geodesic models of quasi-periodic-oscillations as probes of quadratic gravity. *The Astrophysical Journal*, 843(1):25, jun 2017.

[21] Cosimo Bambi. Probing the space-time geometry around black hole candidates with the resonance models for high-frequency QPOs and comparison with the continuum-fitting method. *Journal of Cosmology and Astroparticle Physics*, 2012(09):014–014, sep 2012.

[22] David Hochberg and Matt Visser. Null energy condition in dynamic wormholes. *Physical Review Letters*, 81(4):746–749, jul 1998.

[23] David Hochberg and Matt Visser. Dynamic wormholes, antitrapped surfaces, and energy conditions. *Physical Review D*, 58(4):044021, jul 1998.

[24] Edward Teo. Rotating traversable wormholes. *Physical Review D*, 58(2):024014, jun 1998.

[25] David Hochberg. Lorentzian wormholes in higher order gravity theories. *Physics Letters B*, 251(3):349–354, nov 1990.

[26] Hiroki Fukutaka, Kazuo Ghoroku, and Khoichi Tanaka. Wormholes solutions in higher derivative gravity. *Physics Letters B*, 222(2):191–194, may 1989.

[27] Kazuo Ghoroku and Teruhiko Soma. Lorentzian wormholes in higher-derivative gravity and the weak energy condition. *Physical Review D*, 46(4):1507–1516, aug 1992.

[28] Francisco S. N. Lobo and Miguel A. Oliveira. Wormhole geometries in $f(r)$ modified theories of gravity. *Physical Review D*, 80(10):104012, nov 2009.

[29] Panagiota Kanti, Burkhard Kleihaus, and Jutta Kunz. Wormholes in dilatonic einstein-gauss-bonnet theory. *Physical Review Letters*, 107(27):271101, dec 2011.

[30] Panagiota Kanti, Burkhard Kleihaus, and Jutta Kunz. Stable lorentzian wormholes in dilatonic einstein-gauss-bonnet theory. *Physical Review D*, 85(4):044007, feb 2012.

[31] Georgios Antoniou, Athanasios Bakopoulos, Panagiota Kanti, Burkhard Kleihaus, and Jutta Kunz. Novel einstein–scalar-gauss-bonnet wormholes without exotic matter. *Physical Review D*, 101(2):024033, jan 2020.

[32] Rustam Ibadov, Burkhard Kleihaus, Jutta Kunz, and Sardor Murodov. Wormholes in einstein-scalar-gauss-bonnet theories with a scalar self-interaction potential. *Physical Review D*, 102(6):064010, sep 2020.

[33] Vladimir Dzhunushaliev, Vladimir Folomeev, Christian Hoffmann, Burkhard Kleihaus, and Jutta Kunz. Boson stars with nontrivial topology. *Physical Review D*, 90(12):124038, dec 2014.

[34] Christian Hoffmann, Theodora Ioannidou, Sarah Kahlen, Burkhard Kleihaus, and Jutta Kunz. Spontaneous symmetry breaking in wormholes spacetimes with matter. *Physical Review D*, 95(8):084010, apr 2017.

[35] Christian Hoffmann, Theodora Ioannidou, Sarah Kahlen, Burkhard Kleihaus, and Jutta Kunz. Wormholes immersed in rotating matter. *Physics Letters B*, 778:161–166, mar 2018.

[36] Christian Hoffmann, Theodora Ioannidou, Sarah Kahlen, Burkhard Kleihaus, and Jutta Kunz. Symmetric and asymmetric wormholes immersed in rotating matter. *Physical Review D*, 97(12):124019, jun 2018.

[37] Vladimir Dzhunushaliev, Vladimir Folomeev, Burkhard Kleihaus, and Jutta Kunz. A star harbouring a wormhole at its core. *Journal of Cosmology and Astroparticle Physics*, 2011(04):031–031, apr 2011.

[38] Vladimir Dzhunushaliev, Vladimir Folomeev, Burkhard Kleihaus, and Jutta Kunz. Mixed neutron-star-plus-wormhole systems: Equilibrium configurations. *Physical Review D*, 85(12):124028, jun 2012.

[39] Vladimir Dzhunushaliev, Vladimir Folomeev, Burkhard Kleihaus, and Jutta Kunz. Mixed neutron-star-plus-wormhole systems: Linear stability analysis. *Physical Review D*, 87(10):104036, may 2013.

[40] Ascar Aringazin, Vladimir Dzhunushaliev, Vladimir Folomeev, Burkhard Kleihaus, and Jutta Kunz. Magnetic fields in mixed neutron-star-plus-wormhole systems. *Journal of Cosmology and Astroparticle Physics*, 2015(04):005–005, apr 2015.

[41] Michael S. Morris and Kip S. Thorne. Wormholes in spacetime and their use for interstellar travel: A tool for teaching general relativity. *American Journal of Physics*, 56(5):395–412, may 1988.

[42] A. N. Aliev and D. V. Galtsov. Radiation from relativistic particles in nongeodesic motion in a strong gravitational field. *General Relativity and Gravitation*, 13(10):899–912, oct 1981.

[43] A. N. Aliev, D. V. Gal'tsov, and V. I. Petukhov. Negative absorption near a magnetized black hole: Black hole masers. *Astrophysics and Space Science*, 124(1):137–157, 1986.

[44] L. Landau and E. Lifshitz. *Mechanics*. Pergamon Press, Oxford, 1976.

[45] Paola Rebusco. Twin peaks kHz QPOs: Mathematics of the 3:2 orbital resonance. *Publications of the Astronomical Society of Japan*, 56(3):553–557, jun 2004.

[46] Jiří HorÁk, Marek A. Abramowicz, Vladimír Karas, and Wodzimierz Kluźniak. Of NBOs and kHz QPOs: a low-frequency modulation in resonant oscillations of relativistic accretion disks. *Publications of the Astronomical Society of Japan*, 56(5):819–822, oct 2004.

[47] T Damour and G Esposito-Farese. Tensor-multi-scalar theories of gravitation. *Classical and Quantum Gravity*, 9(9):2093–2176, sep 1992.

[48] Michael Horbatsch, Hector O Silva, Davide Gerosa, Paolo Pani, Emanuele Berti, Leonardo Gualtieri, and Ulrich Sperhake. Tensor-multi-scalar theories: relativistic stars and 3 + 1 decomposition. *Classical and Quantum Gravity*, 32(20):204001, sep 2015.

[49] Daniela D. Doneva and Stoytcho S. Yazadjiev. Topological neutron stars in tensor-multi-scalar theories of gravity. *Physical Review D*, 101(6):064072, mar 2020.

[50] Daniela D. Doneva and Stoytcho S. Yazadjiev. New gauss-bonnet black holes with curvature-induced scalarization in extended scalar-tensor theories. *Physical Review Letters*, 120(13):131103, mar 2018.

[51] Paulo C. C. Freire et al. The relativistic pulsar-white dwarf binary PSR J1738+0333 – II. the most stringent test of scalar-tensor gravity. *Monthly Notices of the Royal Astronomical Society*, 423(4):3328–3343, jun 2012.

[52] John Antoniadis et al. A massive pulsar in a compact relativistic binary. *Science*, 340(6131), apr 2013.

[53] Lijing Shao, Noah Sennett, Alessandra Buonanno, Michael Kramer, and Norbert Wex. Constraining nonperturbative strong-field effects in scalar-tensor gravity by combining pulsar timing and laser-interferometer gravitational-wave detectors. *Physical Review X*, 7(4):041025, oct 2017.

[54] Daniela D. Doneva and Stoytcho S. Yazadjiev. Neutron star solutions with curvature induced scalarization in the extended gauss-bonnet scalar-tensor theories. *Journal of Cosmology and Astroparticle Physics*, 2018(04):011–011, apr 2018.

[55] Paolo Pani, Emanuele Berti, Vitor Cardoso, and Jocelyn Read. Compact stars in alternative theories of gravity: Einstein-Dilaton-Gauss-Bonnet gravity. *Physical Review D*, 84(10):104035, nov 2011.

[56] Robert M. Wald. Black hole entropy is the noether charge. *Physical Review D*, 48(8):R3427–R3431, oct 1993.

[57] Jose Luis Blázquez-Salcedo, Daniela D. Doneva, Jutta Kunz, and Stoytcho S. Yazadjiev. Radial perturbations of the scalarized einstein-gauss-bonnet black holes. *Physical Review D*, 98(8):084011, oct 2018.

[58] Jose Luis Blázquez-Salcedo, Daniela D. Doneva, Sarah Kahlen, Jutta Kunz, Petya Nedkova, and Stoytcho S. Yazadjiev. Axial perturbations of the scalarized einstein-gauss-bonnet black holes. *Physical Review D*, 101(10):104006, may 2020.

[59] IIvan Zh. Stefanov, Stoytcho S. Yazadjiev, and Michail D. Todorov. Phases of 4D scalar – tensor black holes coupled to born – infeld nonlinear electrodynamics. *Modern Physics Letters A*, 23(34):2915–2931, nov 2008.

[60] Daniela D. Doneva, Stoytcho S. Yazadjiev, Kostas D. Kokkotas, and Ivan Zh. Stefanov. Quasinormal modes, bifurcations, and nonuniqueness of charged scalar-tensor black holes. *Physical Review D*, 82(6):064030, sep 2010.

[61] Hector O. Silva, Caio F. B. Macedo, Thomas P. Sotiriou, Leonardo Gualtieri, Jeremy Sakstein, and Emanuele Berti. Stability of scalarized black hole solutions in scalar-gauss-bonnet gravity. *Physical Review D*, 99(6):064011, mar 2019.

[62] Carlos Palenzuela, Enrico Barausse, Marcelo Ponce, and Luis Lehner. Dynamical scalarization of neutron stars in scalar-tensor gravity theories. *Physical Review D*, 89(4):044024, feb 2014.

[63] Masaru Shibata, Keisuke Taniguchi, Hirotada Okawa, and Alessandra Buonanno. Coalescence of binary neutron stars in a scalar-tensor theory of gravity. *Physical Review D*, 89(8):084005, apr 2014.

[64] Mohammed Khalil, Noah Sennett, Jan Steinhoff, and Alessandra Buonanno. Theory-agnostic framework for dynamical scalarization of compact binaries. *Physical Review D*, 100(12):124013, dec 2019.

[65] H. Müther, M. Prakash, and T.L. Ainsworth. The nuclear symmetry energy in relativistic brueckner-hartree-fock calculations. *Physics Letters B*, 199(4):469–474, dec 1987.

[66] B. P. Abbott et al. GW170817: Observation of gravitational waves from a binary neutron star inspiral. *Physical Review Letters*, 119(16):161101, oct 2017.

[67] Jocelyn S. Read, Benjamin D. Lackey, Benjamin J. Owen, and John L. Friedman. Constraints on a phenomenologically parametrized neutron-star equation of state. *Physical Review D*, 79(12):124032, jun 2009.

[68] Daniela D. Doneva, Stella Kiorpelidi, Petya G. Nedkova, Eleftherios Papantonopoulos, and Stoytcho S. Yazadjiev. Charged gauss-bonnet black holes with curvature induced scalarization in the extended scalar-tensor theories. *Physical Review D*, 98(10):104056, nov 2018.